Semiclassical treatment of spinor topological effects in driven inhomogeneous insulators under external electromagnetic fields

Ioannis Petrides[1] and Oded Zilberberg[2]
[1]*Harvard John A. Paulson School of Engineering and Applied Sciences, Harvard University, Cambridge, Massachusetts 02138, USA*
[2]*Department of Physics, University of Konstanz, D-78457 Konstanz, Germany*

(Received 14 April 2022; accepted 12 September 2022; published 26 October 2022)

Introducing internal degrees of freedom in the description of topological insulators has led to a myriad of theoretical and experimental advances. Of particular interest are the effects of periodic perturbations, either in time or space, as they considerably enrich the variety of electronic responses, with examples such as Thouless's charge pump and its higher-dimensional cousins, or higher-order topological insulators. Here, we develop a semiclassical approach to transport and accumulation of general spinor degrees of freedom, such as physical spin, valley, or atomic orbits, in adiabatically driven, weakly inhomogeneous insulators of dimensions 1, 2, and 3, under external electromagnetic fields. Specifically, we derive the spinor current and density up to third order in the spatiotemporal modulations of the system and relate the induced responses to geometrical and topological objects—the spinor-Chern fluxes and numbers—defined over the higher-dimensional phase space of the system, i.e., its combined position-momentum-time coordinates. Furthermore, we provide a connection between our semiclassical analysis and the modern theory of multipole moments by introducing spinor analogs of the electric dipole, quadrupole, and octupole moments. The results are showcased in concrete tight-binding models where spinor transport and accumulation are calculated analytically.

DOI: 10.1103/PhysRevB.106.165130

I. INTRODUCTION

The topological and geometrical aspects of condensed matter systems have yet to be fully explored, even at the single-particle level [1–3]. A prominent platform for probing such physics with electromagnetic fields involves spatially homogeneous electronic insulators, due to the fact that contributions from the Fermi surface vanish. In such gapped systems, the electronic spectrum can be associated with a global quantity defined over the entire momentum space—the topological index. Interestingly, this index manifests in quantized responses to the applied electromagnetic fields, e.g., the Hall effect [4,5] or the Streda response [6]. Following several decades of research, many topological aspects of momentum space are well understood using rigorous mathematical methods, such as K theory [7–10], nonlinear σ model analysis [11–13], and dimensional reduction [2,14,15], that rely on a combination of local symmetries, symmorphic or nonsymmorphic crystalline symmetries [16–18], or even quasiperiodicity [19,20] to classify electronic systems.

In recent years, theoretical and experimental studies in ultracold atoms [21–26], photonics [27–32], mechanical systems [33–40], electrical circuits [41–46], and moiré heterostructures [47] have shown enormous capabilities in simulating exotic quantum phenomena. In particular, the induced responses that arise in systems subject to time-dependent modulations were shown to depend on topological aspects that go beyond the traditional momentum-space description. An archetypical example is Thouless's one-dimensional (1D) charge pump [5,22,23,27,28,48], where the adiabatic and periodic modulation of the system's parameters results in the transport of a quantized amount of charge across the otherwise insulating bulk; such quantization was shown to be related to a first Chern number defined over the combined momentum-time manifold. Taking these concepts to two and three dimensions led to topological charge pumps with high-dimensional topological responses, associated with the second and third Chern numbers, respectively. Such responses have a plethora of corresponding boundary physics, including effects with codimension greater than 1 [2,21,32,49,50].

Complementary to topological charge pumps are the newly found higher-order topological insulators (TIs), where the ground state is characterized by the existence of fractional boundary charges with codimensions greater than 1 [51–59]. Such states can be classified by their electric multipole moments that take quantized values when constrained by symmetries. The appearance of nontrivial electric multipoles and localized charges finds numerous manifestations in crystalline materials [60–64], as well as in photonic lattices [32,65], metamaterials [33,66], electrical circuits [42,43], and superconductors [15,67].

An alternative description of higher-order TIs is found within the semiclassical theory, where physical observables were shown to depend on the topological aspects of the entire phase space, i.e., the combined position-momentum-time manifold [50,68–76]. For example, charge transport and accumulation were shown to depend on geometrical quantities, called Chern fluxes, that become quantized and fractional

when global symmetries are imposed; these are related to quantized changes of the electric multipoles and, hence, to localized charges [77].

Generalizing the description to other internal degrees of freedom beyond charge offers new possibilities in engineering next-generation devices using topological quantum states. For example, the coherent control and manipulation of physical spins finds numerous applications in spintronics and has motivated the search of dissipationless spin currents in quantum dot structures [78], in spin-Hall systems, such as doped GaAs [79–82], in higher-order topological spin models [83,84], and in 1D topological spin pumps [85–89]. The last is the analog of Thouless's 1D charge pump with a direct relation between spin transport and a first spin-Chern number defined over the system's parameter space. However, largely unexplored are the topological signatures of spin observables combined with spatiotemporal modulation in higher dimensions.

Here, we derive the transport and accumulation of general degrees of freedom, dubbed "spinor" degrees, in adiabatically driven, weakly inhomogeneous insulators of dimensions 1, 2, and 3, under external electromagnetic fields. We start by reviewing the semiclassical description of crystalline materials and show how the equations of motion of an electron wave packet lead to charge transport and accumulation. We then extend this framework to include spinor degrees of freedom and derive the spinor transport and accumulation up to third order in perturbation theory. We find that these are related to topological and geometrical quantities—the spinor-Chern numbers and fluxes—that are defined over the entire phase space of the system. Similar to charge responses, we obtain generalizations of topological spinor pumps, the spinor-Hall effect, spinor-higher-order TIs, and spinor-axion responses. Finally, we decompose the derived corrections into spinor analogs of the electric multipole moments, thus establishing a direct relation between macroscopic properties of the material and the spinor-topological aspects of phase space. We showcase our results in concrete tight-binding Hamiltonians, where we focus on physical spin.

II. SEMICLASSICAL APPROACH

In this section, we review the semiclassical description of electrons in insulating materials under general perturbing fields and show how the geometrical properties of phase space manifest as corrections to charge transport and accumulation [50,68–75]. Depending on the dimensionality of the system, the equations of motion will include effects up to third order in the perturbing fields [5,50,73,90], as it is only at this order that electronic responses of three-dimensional (3D) materials can be well captured. Once the semiclassical theory of the charge degree of freedom is reviewed, we will extend it to general spinor degrees and straightforwardly apply it to dimensions 1, 2, and 3 in Sec. III.

The semiclassical theory offers an intuitive picture for describing transport and accumulation of charged particles moving in insulators that are subject to weak spatiotemporal modulations. It describes the particles as wave packets that adiabatically move in phase space with respect to a local eigenbasis [see Fig. 1(a)]. Specifically, the wave packet is assumed to have well-defined center-of-mass coordinates

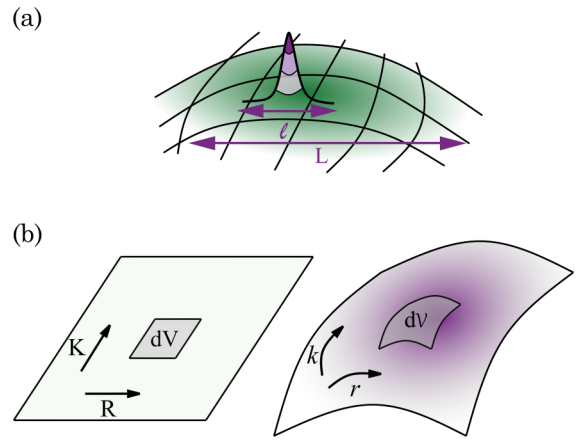

FIG. 1. Semiclassical theory. (a) The electron is represented by a wave packet with well-localized center-of-mass coordinates that moves in the phase space of the system. Its trajectory is defined by the anomalous forces and velocities that arise due to the geometry of phase space [cf. Eq. (2)]. The length scale L defined by the perturbing fields is assumed to be much longer than the width l of the wave packet, such that a local Hamiltonian can always be defined [cf. Eq. (1)]. (b) For canonical coordinates, the phase-space volume element is constant. When transforming to physical coordinates, it is modified according to the curvature tensors appearing in the equations of motion [cf. Eq. (7)].

$\boldsymbol{\xi} = (\boldsymbol{r}, \boldsymbol{k}, t)$, where $\boldsymbol{r}$ denotes the position, $\boldsymbol{k}$ the crystal's quasimomentum, and t the time, such that its dynamics can be perturbatively expanded at small distances as

$$\hat{H} \approx \hat{H}_0 + \hat{H}'. \tag{1}$$

Here, $\hat{H}_0$ is the unperturbed Hamiltonian and $\hat{H}'$ are higher-order corrections. In this case, the wave packet is built directly from the N eigenstates

$$|n(\boldsymbol{\xi})\rangle \approx |n_0\rangle + |n'\rangle$$

of a set of isolated energy bands of $\hat{H}$, where $|n_0\rangle$ are the eigenstates of $\hat{H}_0$ and $|n'\rangle$ are higher-order corrections.

For more details on the construction of the wave packet and the derivation of its equations of motion up to third order, see Refs. [50,68–75,91,92] and Appendix A. Here, we directly use the resulting velocity and force equations describing the center-of-mass evolution,

$$\begin{aligned} \dot{\underline{r}}^i &= \partial_{k_i}\mathcal{E} - \Omega_{k_i k_j}\dot{\underline{k}}_j - \Omega_{k_i r_j}\dot{\underline{r}}_j - \Omega_{k_i t}, \\ \dot{\underline{k}}^i &= -\partial_{r_i}\mathcal{E} + \Omega_{r_i k_j}\dot{\underline{k}}_j + \Omega_{r_i r_j}\dot{\underline{r}}_j + \Omega_{r_i t}, \end{aligned} \tag{2}$$

where $\underline{\boldsymbol{r}}_{nm} = \langle n|\hat{\boldsymbol{r}}|m\rangle$ and $\underline{\boldsymbol{k}}_{nm} = \langle n|\hat{\boldsymbol{k}}|m\rangle$ are the matrix representations of the wave packet's center-of-mass position and momentum, the energy dispersion $\mathcal{E}^{nm} = \langle n(\boldsymbol{\xi})|\hat{H}_0 + \hat{H}'|m(\boldsymbol{\xi})\rangle$ is calculated up to a sufficiently high order in perturbation theory, and Einstein's summation convention is assumed. The curvature tensors are defined as

$$\Omega_{\xi_\mu\xi_\nu} = \partial_{\xi_\mu}\mathcal{A}_{\xi_\nu} - \partial_{\xi_\nu}\mathcal{A}_{\xi_\mu}, \tag{3}$$

where

$$\mathcal{A}^{nm}_{\xi_\mu} = \langle n(\boldsymbol{\xi})|i\partial_{\xi_\mu}|m(\boldsymbol{\xi})\rangle \tag{4}$$

is the so-called connection and ξ_μ denotes the μth coordinate in phase space. Depending on the particular directions involved, we dub $\Omega_{k_ik_j}$ the "momentum (Berry) curvature" and $\Omega_{r_ir_j}$ the "position curvature," while $\Omega_{k_ir_j}$, Ω_{k_it}, and Ω_{r_it} are dubbed the mixed momentum-position, momentum-time, and position-time curvatures. Without loss of generality, throughout the paper we assume that the connection in position coordinates is given by the sum of the electromagnetic vector potential $\boldsymbol{A}$ and deformation vector potential $\boldsymbol{V}$, i.e., $\mathcal{A}_{r_i} = -A_i + V_i$. For simplicity, we further assume that $\boldsymbol{V}$ gives rise to a flat curvature in position-time coordinates, as such effects are equivalently described by the magnetic $\Omega_{r_ir_j} \equiv B_{ji}$ and electric $\Omega_{tr_i} \equiv E_i$ fields (up to a minus sign difference).

The equations of motion (2) exhibit the usual dependence on the group velocity $\frac{\partial \mathcal{E}}{\partial k_i}$ [93] and force $\frac{\partial \mathcal{E}}{\partial r_i}$, while the curvature tensors $\Omega_{\xi_\mu\xi_\nu}$ appear as "anomalous velocity" and "anomalous force" terms that modify the trajectories of the wave packet depending on the geometrical structure of phase space [94–96]. For example, the anomalous velocity $\Omega_{k_ik_j}\dot{k}_j$ can be understood as a momentum-space analog of the magnetic Lorentz force where $\Omega_{k_ik_j}$ plays the role of a magnetic field in momentum space. This gives rise to the quantum Hall effect [4,5] and can be used to map out the distribution of the momentum curvature over energy bands [94–96].

Assuming that energy bands are uniformly filled up to some spectral gap, the associated charge density and current read

$$\rho_{\text{particle}} = \int_{\mathbb{T}^d} \frac{d^dk}{(2\pi)^d} \operatorname{Tr} D(\boldsymbol{\xi}), \tag{5}$$

$$\boldsymbol{j}_{\text{particle}} = \int_{\mathbb{T}^d} \frac{d^dk}{(2\pi)^d} \operatorname{Tr} D(\boldsymbol{\xi})\underline{\dot{\boldsymbol{r}}}, \tag{6}$$

respectively, where the integral runs over the entire d-dimensional Brillouin zone denoted by the d-torus $\mathbb{T}^d$, the trace is performed over the set of occupied states, and $D(\boldsymbol{\xi})$ is the modified density of states. The latter is a consequence of the underlying geometry of phase space, as it takes into account the change in the number of available states when nontrivial curvature tensors are included [73,74,97–100] [see Fig. 1(b)]. This change can be classically understood from Liouville's theorem, which states that if the dynamics are Hamiltonian, the phase-space volume element is conserved when transforming from *canonical* to *physical* coordinates. Using generalized Peierls substitutions [97–100], we note that the physical coordinates $(\boldsymbol{r}, \boldsymbol{k})$ are related to the canonical coordinates $(\boldsymbol{R}, \boldsymbol{K})$ by $\boldsymbol{r} = \boldsymbol{R} - \boldsymbol{\mathcal{A}}_k$ and $\boldsymbol{k} = \boldsymbol{K} - \boldsymbol{\mathcal{A}}_r$, where $\boldsymbol{\mathcal{A}}_r$ ($\boldsymbol{\mathcal{A}}_k$) is the position (momentum) connection [cf. Eq. (4)]. The extent by which the physical coordinates deviate from being canonical is quantified by the curvature tensors $\Omega_{\xi_\mu\xi_\nu}$ [cf. Eq. (3)], and the change of phase-space volume element is described by the Jacobian of the transformation [98], given by

$$D(\boldsymbol{\xi}) = \sqrt{\det\begin{pmatrix} \underline{\Omega}^{(r)} & -\mathbb{1} - \underline{\Omega}^{(kr)} \\ \mathbb{1} + \underline{\Omega}^{(kr)} & \underline{\Omega}^{(k)} \end{pmatrix}}, \tag{7}$$

where $\mathbb{1}$ is the identity matrix and $\underline{\Omega}^{(k)}$, $\underline{\Omega}^{(r)}$, and $\underline{\Omega}^{(kr)}$ are antisymmetric matrices with components $\Omega_{k_ik_j}$, $\Omega_{r_ir_j}$, and $\Omega_{k_ir_j}$, respectively. The total change in phase-space volume is found by tracing $D(\boldsymbol{\xi})$ over the occupied energy bands, as done in Eq. (5).

In fermionic systems, the particle density ρ_{particle} is proportional to the charge accumulation induced by charged carriers. However, we emphasize that the semiclassical formalism can straightforwardly be applied to a uniformly filled set of bands of bosons [74]. As we will see in Sec. III, the semiclassical approximation of the particle density at first order in perturbing fields gives rise to a quantized particle accumulation with codimensions 1, i.e., the ground state supports states that are localized in one dimension but extended in the other directions. This is closely related to the soliton solutions found in Ref. [101] in the context of high-energy physics. At second order it results in the Streda formula [6], and in a quantized charge accumulation with codimensions 2 [15,51,60,66,77,102]. Finally, third-order terms give rise to axion responses in the spatial domain [2,14,103], and quantized charge accumulation with codimensions 3 [55].

Next, the particle current of Eq. (6) is calculated by integrating the corresponding velocity $\underline{\dot{r}}^i$ over the entire d-dimensional Brillouin zone, weighted by the density of states $D(\boldsymbol{\xi})$. The velocity of the wave packet in phase space is found by recursively solving differential equations (2) up to a particular order, while the density of states is given in Eq. (7). The induced corrections are hence classified into density-type, Lorentz-type, or mixed Lorentz-density-type responses, depending whether they result from the density of states, the velocity, or a combination of the two [21,32,50].

As we will see in Sec. III, the corrections to the particle current of an insulating ground state give rise to Thouless's 1D charge pump [5,27,48] and to the quantum Hall effect [4,5], both having a characteristic first Chern number response. At higher orders, we recover two-dimensional (2D) topological charge pumps and axion field effects, where the associated responses are determined by a second Chern number [2,14,49]. Finally, third-order corrections give rise to 3D topological charge pumps and a third Chern number response [50,75].

A. Spinor current and density

We generalize the semiclassical description of charge transport and accumulation to other quantum numbers, which we generally dub "spinor degrees of freedom." These degrees can represent various particle properties, e.g., charge, physical spin, valley index, or any other internal degree. The derivation of the current and density follows a similar procedure, with the difference now that all quantities are defined with respect to the spinor operator $\hat{\mathcal{S}}$:

$$\rho_{\hat{\mathcal{S}}} = \int_{\mathbb{T}^d} \frac{d^dk}{(2\pi)^d} \operatorname{Tr} \underline{\mathcal{S}} D(\boldsymbol{\xi}), \tag{8}$$

$$\boldsymbol{j}_{\hat{\mathcal{S}}} = \int_{\mathbb{T}^d} \frac{d^dk}{(2\pi)^d} \operatorname{Tr} \underline{\mathcal{S}} D(\boldsymbol{\xi})\underline{\dot{\boldsymbol{r}}}, \tag{9}$$

where $\underline{\mathcal{S}}$ is the matrix representation of the operator $\hat{\mathcal{S}}$ with components $\underline{\mathcal{S}}^{nm} = e_s\langle n(\boldsymbol{\xi})|\hat{\mathcal{S}}|m(\boldsymbol{\xi})\rangle$, and e_s is the value of the associated spinor charge. Even though the formalism is

generic to any operator $\hat{\mathcal{S}}$, here we focus on physical spins in concrete tight-binding models and analytically calculate the induced responses. By exploiting the full breadth of these corrections, we engineer dynamical systems, where the quantized spin transport and accumulation are related to nontrivial topological indices defined over the system's phase space.

B. Geometrical definitions

Before continuing, it is useful to define general geometrical and topological quantities in phase space that will later appear as physical corrections to spinor transport and accumulation. For a uniformly occupied set of eigenstates, we define the spinor analogs of Chern numbers, sub-Chern numbers, and Chern fluxes in arbitrary dimensions. Unless otherwise stated, we assume $\boldsymbol{\xi}$ can be mapped on a torus.

First, the first spinor-Chern number is defined as

$$c_1 = \frac{1}{2\pi}\int_{\mathbb{T}^2} d^2\xi \,\mathrm{Tr}\underline{\mathcal{S}}\Omega_{\xi_\mu\xi_\nu}, \tag{10}$$

where the integral is taken over a 2D closed surface in the (ξ_μ, ξ_ν) plane, denoted here by $\mathbb{T}^2$. We note that the degree of freedom $\underline{\mathcal{S}}$ is used in a generic way to represent any type of quantum number. For example, when it corresponds to physical spins, this topological index—called the first spin-Chern number—takes integer values and governs the robust quantization of spin conductance in the 2D spin-Hall effect [79–82,104–106], and the quantized spin transport in 1D topological spin pumps [89]. Alternatively, when $\underline{\mathcal{S}}$ is proportional to the identity, the above equation is reduced to the well-known first Chern number which determines the 2D quantum Hall effect [4,5], the center-of-mass drift of an atomic cloud [107], the dynamical vortex trajectories of a quenched cold-atom gas [108], the heating rate of shaken systems [109–111], and the charge transport of 1D topological charge pumps [22,23].

The second spinor-Chern number emerges in a four-dimensional (4D) manifold and it is given by the antisymmetric product of two 2-forms,

$$c_2 = \frac{1}{32\pi^2}\int_{\mathbb{T}^4} d^4\xi \,\epsilon^{\alpha\beta\gamma\delta}\mathrm{Tr}\underline{\mathcal{S}}\Omega_{\xi_\alpha\xi_\beta}\Omega_{\xi_\gamma\xi_\delta}, \tag{11}$$

where $\mathbb{T}^4$ denotes the 4D closed manifold and where $\epsilon^{\alpha\beta\gamma\delta}$ is the Levi-Cività symbol defined in the 4D $\boldsymbol{\xi}$-coordinate space. When $\underline{\mathcal{S}}$ corresponds to the charge degree of freedom, it is exactly the second Chern number appearing in the nonlinear 4D quantum Hall response of a system with four spatial dimensions [14,73,90,112,113], in the bulk transport of two-dimensional topological pumps [21], as well as in the dynamics of internal states in Bose-Einstein condensates [114,115].

Finally, the relevant topological invariant in a six-dimensional (6D) manifold is the third spinor-Chern number

$$c_3 = \frac{1}{(2\pi)^3}\int_{\mathbb{T}^6} d^6\xi \,\frac{1}{2^3\cdot 3!}\epsilon^{\alpha\beta\gamma\delta\epsilon\zeta}\mathrm{Tr}\underline{\mathcal{S}}\Omega_{\xi_\alpha\xi_\beta}\Omega_{\xi_\gamma\xi_\delta}\Omega_{\xi_\epsilon\xi_\zeta}, \tag{12}$$

where the 6D $\boldsymbol{\xi}$-coordinate space is denoted by $\mathbb{T}^6$ and where we have introduced the 6D Levi-Cività symbol $\epsilon^{\alpha\beta\gamma\delta\epsilon\zeta}$. The third spinor-Chern number is inherently a 6D topological invariant as it vanishes for systems with fewer than six dimensions. It underlies the 6D quantum Hall effect and it manifests in the charge transport of 3D topological charge pumps [50].

For a given set of $\boldsymbol{\xi}$ coordinates, it is important to remember that all lower-dimensional topological indices can still be defined, but now with respect to the various subdimensional manifolds [116]. In practice, each set of states in a D-dimensional coordinate space is characterized by a set of first spinor-Chern numbers, associated with each possible 2D plane; a set of second spinor-Chern numbers, associated with each possible 4D subvolume; all the way up to the $D/2$-th spinor-Chern number (where D is even) that characterizes the entire manifold of states. We dub such lower-dimensional quantities "sub-spinor-Chern numbers." Notably, these are not integer valued as the integrals run over the entire D-dimensional space. Instead, they depend both on the relevant lower-dimensional spinor-Chern numbers as well as on the volume of the coordinate space perpendicular to the selected submanifold [73,74].

Analogously to the spinor-Chern numbers, the first spinor-Chern flux is defined as

$$\Phi_1 = \frac{1}{2\pi}\int_{\mathcal{C}} d\mathcal{C}\,\mathrm{Tr}\,\underline{\mathcal{S}}\Omega_{\xi_\mu\xi_\nu}, \tag{13}$$

where $\Omega_{\xi_\mu\xi_\nu}$ is the curvature in the (ξ_μ, ξ_ν) plane, and $\mathcal{C}$ is an *open* integration domain with volume element $d\mathcal{C}$. This quantity is related to the first spinor-Chern number, but now the integration domain runs over a subvolume $\mathcal{C}$ of the entire two-dimensional manifold.

Going up in dimensionality, the second and third spinor-Chern fluxes are defined as

$$\Phi_2 = \frac{1}{32\pi^2}\int_{\mathcal{C}} d\mathcal{C}\epsilon^{\mu\nu\sigma\rho}\,\mathrm{Tr}\,\underline{\mathcal{S}}\Omega_{\xi_\mu\xi_\nu}\Omega_{\xi_\sigma\xi_\rho}, \tag{14}$$

$$\Phi_3 = \frac{1}{(2\pi)^3}\int_{\mathcal{C}} d\mathcal{C}\frac{1}{2^3\cdot 3!}\epsilon^{\mu\nu\sigma\rho\gamma\delta}\,\mathrm{Tr}\,\underline{\mathcal{S}}\Omega_{\xi_\mu\xi_\nu}\Omega_{\xi_\sigma\xi_\rho}\Omega_{\xi_\gamma\xi_\delta}, \tag{15}$$

where $\mathcal{C}$ is the associated integration domain with volume element $d\mathcal{C}$. In the definitions of the spinor-Chern fluxes, the integration domain $\mathcal{C}$ does not cover the entire manifold; hence, such expressions are generally not quantized. However, as we will later see, global symmetries can constrain the allowed values of these quantities to support only discrete fractions.

In the following, we will use the terms "spin-Chern number" to indicate the case where $\hat{\mathcal{S}}$ corresponds to physical spin, "Chern number" when $\hat{\mathcal{S}}$ corresponds to charge, and "spinor-Chern number" whenever we consider general degrees (analogously for the remaining geometrical definitions).

III. DRIVEN, INHOMOGENEOUS INSULATORS UNDER ELECTROMAGNETIC FIELDS

In this section, we use the semiclassical approach (cf. Sec. II) to calculate the spinor transport and accumulation induced by weakly perturbing a crystal in momentum, position, and time. In practice, these perturbations correspond to external electromagnetic fields, weak spatial inhomogeneities, and adiabatic drives, respectively. We start by calculating

the quantized spinor transport in an adiabatically driven one-dimensional Hamiltonian where we obtain the same results as originally derived for a spin model in Ref. [89] using a quantum-mechanical approach. Then, we derive the corrections to the density of states and calculate the spinor accumulation on a domain wall induced by weakly modulating the system in space. Finally, we generalize the description to dimensions 2 and 3, and showcase the results in concrete tight-binding models where the responses are calculated analytically.

Our semiclassical derivation shows that spinor (and in particular spin) transport and accumulation are proportional to geometrical and topological quantities defined over the system's phase space—the spinor-Chern numbers and spinor-Chern fluxes. We explore the various manifestations of these quantities in driven, inhomogeneous crystals under electromagnetic fields and, in particular, relate them to the spatiotemporal modulations of spinor analogs of the electric multipole moments. As such, we provide a complete description of transport and accumulation of noninteracting electrons in perturbed crystalline insulators and illuminate a fundamental connection between the topological aspects of phase space and physical observables.

A. In one dimension

In the following, we derive the corrections to the spinor current and density of a one-dimensional adiabatically driven insulator with weak spatial inhomogeneities using the semiclassical approach of Sec. II. First, we calculate the spinor transport in a periodically driven Hamiltonian and show its relation to the temporal change of a spinor-dipole moment. Similar to the 1D Thouless charge pump, the spinor transport after a cycle is found to be quantized and equal to a first spinor-Chern number defined in the phase space of the system. We extend these results to derive the spinor accumulation on a domain wall created by smoothly modulating the Hamiltonian in position and find that it is related to a geometrical property of phase space—the first spinor-Chern flux. Even though such a quantity is generally not quantized, we show that under global symmetry constraints it can become quantized and lead to a fractional spinor accumulation localized at the interface. The relation to the spatial modulation of the spinor-dipole moment is also discussed.

To illustrate our results, we consider a tight-binding model describing spinful electrons moving on a 1D lattice [see Fig. 2(a)], with Hamiltonian

$$H = H_{\mathrm{KE}} + H_{\mathrm{d}} + H_{\mathrm{h}} + H_{\mathrm{SO}}. \tag{16}$$

The first term is the kinetic energy, given by

$$H_{\mathrm{KE}} = J \sum_{n,\alpha} (c^{\dagger}_{n+1,\alpha} c_{n,\alpha} + \mathrm{H.c.}), \tag{17}$$

where J is the hopping amplitude, n is the position vector, $\alpha = \{\uparrow, \downarrow\}$ is the spin index, and the lattice spacing is taken to be unity. The kinetic energy term describes hopping of electrons with spin α between neighboring sites. The hopping

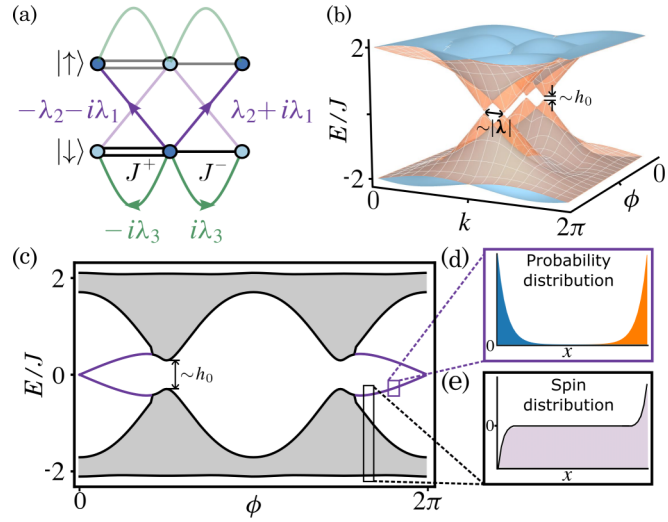

FIG. 2. The model Hamiltonian in one dimension. (a) Sketch of the tight-binding model [cf. Eq. (16)]. Electrons with spin α tunnel to the nearest neighbor with amplitude $J^{\pm} = J \pm \Delta J$, denoted by single or double black lines. The spin-orbit coupling is denoted by the purple and green lines. The light (dark) blue sites denote a staggered potential with positive (negative) sign. (b) The bulk spectrum of $H(k, \phi)$ [cf. Eq. (22)] as a function of quasimomentum k and the internal parameter ϕ. The spectrum is composed by four bands that become degenerate at the high-symmetry points. (c) The open boundary spectrum of the Hamiltonian showing bulk (gray), and codimension-1 (purple) states. (d) The probability distribution of the two lowest energy boundary modes shown in blue and orange. Each state is localized at opposite boundaries, resulting in a vanishing electric dipole moment. (e) The spin density of the ground state at half filling showing spin accumulation at the boundary. For the simulations in (c), (d), and (e) we have used $J/10 = \lambda_1 = \lambda_2 = \lambda_3 = J - \Delta J = 0.1$, and $h_0 = 0.5$, while for (b) we have used $h_0 = 0.05$ to accentuate the effect of spin-orbit interaction.

amplitudes are dimerized by the second term in H, given by

$$H_{\mathrm{d}} = \sum_{n,\alpha} (-1)^n \Delta J (c^{\dagger}_{n+1,\alpha} c_{n,\alpha} + \mathrm{H.c.}). \tag{18}$$

The next term is a staggered on-site potential

$$H_{\mathrm{h}} = h \sum_{n,\alpha,\beta} (-1)^n \tau_z^{\alpha\beta} c^{\dagger}_{n,\alpha} c_{n,\beta}, \tag{19}$$

that couples antiferromagnetically to the spin. Finally, the last term is given by

$$H_{\mathrm{SO}} = \sum_{n,\alpha,\beta} i\boldsymbol{\lambda} \cdot \boldsymbol{\tau}^{\alpha\beta} (c^{\dagger}_{n+1,\alpha} c_{n,\beta} - c^{\dagger}_{n,\alpha} c_{n+1,\beta}), \tag{20}$$

where $\boldsymbol{\lambda} = \{\lambda_1, \lambda_2, \lambda_3\}$ is a vector characterizing the spin-orbit interaction and $\boldsymbol{\tau} = \{\tau_x, \tau_y, \tau_z\}$ are the Pauli matrices representing the spin degree.

The tight-binding model (16) is based on the antiferromagnetic spin-$\frac{1}{2}$ chain describing a class of crystalline materials that can be manipulated by external electromagnetic fields [88,89]. For example, metallic ferromagnetic compounds, such as Cu benzoate [117,118] and Yb_4As_3 [119], develop a staggered on-site potential when a perpendicular *uniform* magnetic field is applied; as a consequence, the material

becomes insulating. This is due to the Néel ground state induced by the competition between Dzyaloshinskii-Moriya interactions and a nonzero gyromagnetic tensor. Additionally, ferroelectric materials, such as MnI_2 and oxides ABO_2 with $A = $ Cu, Ag, Li, or Na and $B = $ Cr or Fe, were shown to have an exchange interaction that depends on the applied electric field [120–123]. The ferroic properties of engineered materials can be deployed in the design of experiments where electromagnetic fields act as control knobs to the system's parameters.

Motivated by the above discussion, we assume that the dimerization amplitude and staggered on-site potential depend on an external parameter ϕ through

$$\Delta J = \Delta J^0 \cos(\phi) \quad \text{and} \quad h = h_0 \sin(\phi), \tag{21}$$

where ΔJ^0 and h_0 are constants. Furthermore, we assume that spatiotemporal variations of ϕ are smooth enough such that the dynamics are well approximated by the first-order semiclassical equations (cf. Sec. II). The bulk spectrum of the Hamiltonian as a function of the external parameter ϕ is calculated by introducing periodic boundary conditions and applying Bloch's theorem to obtain the diagonalized Hamiltonian in terms of the quasimomentum k.

Since the dimerization by ΔJ enlarges the unit cell by an additional orbital index, we express the Bloch Hamiltonian on a cross product of Pauli matrices, representing the combination of spin $\boldsymbol{\tau}$ and orbital degrees $\boldsymbol{\sigma}$. In a suitable gauge, this is given by

$$H(k, \phi) = \boldsymbol{d} \cdot \boldsymbol{\gamma} + \boldsymbol{D} \cdot \boldsymbol{\Gamma}, \tag{22}$$

where

$$\begin{aligned} \boldsymbol{d} &= \{h, J^+ + J^- \cos(k), J^- \sin(k)\}, \\ \boldsymbol{D} &= \{\lambda_1 \sin(k), -\lambda_1 + \lambda_1 \cos(k), \lambda_2 \sin(k), \\ &\quad -\lambda_2 + \lambda_2 \cos(k), \lambda_3 \sin(k), -\lambda_3 + \lambda_3 \cos(k)\} \end{aligned} \tag{23}$$

are real-valued vectors with $J^\pm = J \pm \Delta J$,

$$\boldsymbol{\gamma} = \{\tau_z \otimes \sigma_z, \mathbb{1} \otimes \sigma_x, \mathbb{1} \otimes \sigma_y\} \tag{24}$$

are three 4×4 anticommuting Hermitian matrices $\{\gamma_\mu, \gamma_\nu\} = 2\delta_{\mu\nu}$, and

$$\begin{aligned} \boldsymbol{\Gamma} = \{&\tau_x \otimes \sigma_x, \tau_x \otimes \sigma_y, \tau_y \otimes \sigma_x, \\ &\tau_y \otimes \sigma_y, \tau_z \otimes \sigma_x, \tau_z \otimes \sigma_y\} \end{aligned} \tag{25}$$

are six 4×4 Hermitian matrices representing the spin-orbit interaction.

The bulk energy spectrum of the Bloch Hamiltonian (22) has four bands which can be intuitively described in the low-energy limit by displaced Dirac-like cones in the (k, ϕ) parameter space [see Fig. 2(b)]. The ground state at half filling is conducting only when $h = \Delta J = 0$, while a nonzero dimerization parameter ΔJ or staggered potential h induces a gap around zero energy. The spectrum has a twofold degeneracy in the entire Brillouin zone when $|\boldsymbol{\lambda}| = 0$, which is lifted to isolated points when $|\boldsymbol{\lambda}| > 0$.

The open boundary spectrum of the Hamiltonian is composed by the aforementioned bulk bands, in addition to two degenerate pairs of codimension-1 states [see Fig. 2(c)]. Each pair disperses as a function of ϕ and merges into the bulk bands by crossing the gap. The probability distribution of these states is fully localized on the boundary with an exponential decay depending on the proximity to the bulk bands. It is important to note that each pair has states localized at *opposite* boundaries; hence, their combination induces a zero net charge polarization [see Fig. 2(d)]. On the other hand, the spin density associated to the operator $\hat{\mathcal{S}} = \tau_z \otimes \mathbb{1}$ exhibits spin localization at the boundaries and, hence, induces a nonzero spin polarization [see Fig. 2(e)].

Determining the global symmetries of the system is crucial when characterizing the band structure. For $h = 0$, Hamiltonian (22) has both time-reversal (TR) symmetry $\Theta = i\mathbb{K}\tau_y \otimes \mathbb{1}$ and chiral symmetry $\chi = \mathbb{1} \otimes \sigma_z$ for any value of ΔJ. On the other hand, the system has only TR symmetry in the entire parameter space, i.e.,

$$\Theta^{-1} H(k, \phi) \Theta = H(-k, -\phi), \tag{26}$$

that is preserved for any value of $|\boldsymbol{\lambda}|$, h, and ΔJ. As such, the ground state can be decomposed into "spin sectors," namely,

$$\begin{aligned} |\psi^1(k, \phi)\rangle &= \Theta |\psi^2(-k, -\phi)\rangle, \\ |\psi^2(k, \phi)\rangle &= -\Theta |\psi^1(-k, -\phi)\rangle, \end{aligned} \tag{27}$$

formed by the TR-invariant partners in the (k, ϕ) parameter space. Classifying the topological properties of Hamiltonians depending on their dimensionality and symmetries has been well studied using various theoretical methods [2,7–13]. In our case, the parameter space of the system provides an increased dimensionality that, in fact, can be ascribed a $\mathbb{Z}_2$ index. Below, we show that this topological invariant appears as a first-order correction to the spin transport and accumulation induced by an adiabatic drive, or weak inhomogeneities.

1. Transport

The 1D model of Eq. (16) can be adiabatically pumped by slowly changing the external parameter $\phi(t)$ over time, i.e., by temporally modulating the on-site energy and hopping terms in a periodic fashion [cf. Eq. (21)]. At each time t, the Hamiltonian is assumed to be diagonalized by a set of instantaneous bands, which now define a curvature tensor in the momentum-time coordinates $\Omega^{nm}_{kt} = i\dot{\phi}(\langle \partial_\phi n | \partial_k m \rangle - \langle \partial_k n | \partial_\phi m \rangle)$, where $|n\rangle$ denotes the set of occupied Bloch bands. The spinor current associated to the ground state at half filling [cf. Eq. (9)] is given by

$$j_{\hat{\mathcal{S}}} = \frac{1}{2\pi} \int_{\mathbb{T}^1} dk \, \mathrm{Tr} \, \underline{\mathcal{S}} \Omega_{tk}, \tag{28}$$

where $\hat{\mathcal{S}} = \mathbb{1} \otimes \mathbb{1}$ $(= \sigma_z \otimes \mathbb{1})$ is the charge (physical spin) degree of freedom and the integration of the momentum k is over a $\mathbb{T}^1$-torus representing the entire 1D Brillouin zone.

When the time evolution is periodic, the spinor transport after a pump period T, taken to be unity for simplicity, is equal to

$$\Delta q_{\hat{\mathcal{S}}} = \int_0^T dt \, j_{\hat{\mathcal{S}}} =: c_1. \tag{29}$$

Since the integration is over the closed momentum-time manifold, the transport of $\Delta q_{\hat{\mathcal{S}}}$ spinor charges associated to $\hat{\mathcal{S}}$ is proportional to a first spinor-Chern number $c_1 \sim \int_{\mathbb{T}^2} dk d\phi \, \mathrm{Tr} \, \underline{\mathcal{S}} \Omega_{k\phi}$ defined in the (k, ϕ) parameter space.

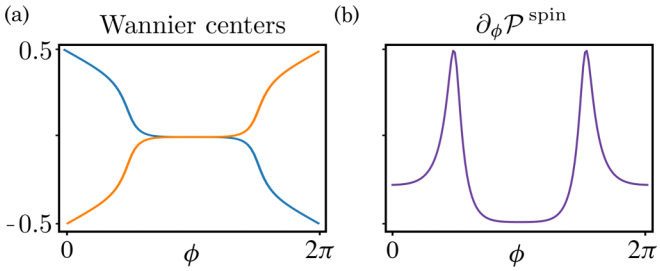

FIG. 3. Wannier centers and polarization. (a) The Wannier centers of the two occupied bands as a function of the external parameter ϕ (cf. Appendix B). Each center "winds" around the unit cell after each cycle. Crucially, the sum of the two vanishes as expected for the charge degree of freedom, i.e., when $\hat{\mathcal{S}} = \mathbb{1} \otimes \mathbb{1}$, but becomes nonzero for physical spin $\hat{\mathcal{S}} = \tau_z \otimes \mathbb{1}$. (b) The derivative of the spin-dipole moment with respect to the external parameter ϕ. The area under the graph is an integer equal to 1, and is related to the first spin-Chern number of the (k, ϕ) parameter space [cf. Eq. (32)]. For the simulations we have used $J/10 = J - \Delta J = h_0/5 = 0.1$, and $\sum_i |\boldsymbol{\lambda}| = 0$.

Following the modern approach to the definition of polarization, the bulk spinor transport must be induced by the temporal gradient of the associated spinor-dipole moment density $\mathcal{P}^{\hat{\mathcal{S}}}$ (cf. Appendix B), i.e.,

$$\Delta q_{\hat{\mathcal{S}}} = \int_T dt \dot{\mathcal{P}}^{\hat{\mathcal{S}}}. \tag{30}$$

For example, when $\hat{\mathcal{S}} = \mathbb{1} \otimes \mathbb{1}$ it corresponds exactly to the electric dipole moment, while for $\hat{\mathcal{S}} = \tau_z \otimes \mathbb{1}$ it is the polarization of physical spin [89]. Comparing with Eq. (29), the first spinor-Chern number c_1 is identified with the contribution from a temporally modulated spinor-dipole moment density, i.e.,

$$c_1 \stackrel{!}{=} \int_T dt \dot{\mathcal{P}}^{\hat{\mathcal{S}}}. \tag{31}$$

The above equality is a natural outcome of the semiclassical formalism: it relates a topological quantity in the system's parameter space—the first spinor-Chern number c_1—to a macroscopic property of the material—the rate of change of the spinor-dipole moment $\mathcal{P}^{\hat{\mathcal{S}}}$.

For the Bloch Hamiltonian of Eq. (22), the first Chern number associated to the charge degree, i.e., when $\hat{\mathcal{S}} = \mathbb{1} \otimes \mathbb{1}$, is identically zero due to the trace properties of the $\boldsymbol{\gamma}$ matrices. Indeed, the electric dipole moment is decomposed into two equal but opposite contributions that originate from the two occupied Bloch states [see Fig. 3(a)]. Each set of negative-energy (equivalently for positive-energy) bands can be written as a direct sum of two orthogonal eigenvectors that are mixed according to the strength of the spin-orbit interaction $\boldsymbol{\lambda}$. Importantly, TR symmetry allows for the decomposition of the polarization into contributions from the two spin sectors [cf. Eq. (27)], where each sector "winds" as a function of the external parameter ϕ. As these contributions have opposite signs, the net electric dipole moment vanishes—a consequence of TR symmetry.

On the other hand, the transport of physical spin, i.e., when $\hat{\mathcal{S}} = \tau_z \otimes \mathbb{1}$, calculated using the eigenvectors of Appendix C, becomes

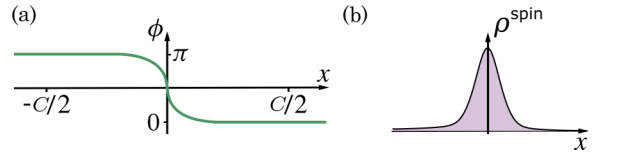

FIG. 4. (a) The domain wall created by the parameter $\phi(r)$. Also shown, the region C enclosing the domain wall. (b) Sketch of the spin accumulation supported on the domain wall.

$$c_1 = \frac{1}{4\pi} \int_{\mathbb{T}^2} d\phi dk \hat{\mathbf{d}} \cdot (\partial_k \hat{\mathbf{d}} \wedge \partial_\phi \hat{\mathbf{d}}) = 1, \tag{32}$$

where $\hat{\boldsymbol{d}} = \boldsymbol{d}/|\boldsymbol{d}|$ and, now, the integration runs over a $\mathbb{T}^2$-torus representing the momentum space and the periodic time evolution. Importantly, the first-order contributions to the first spin-Chern number (32) from a nonzero spin-orbit interaction $|\boldsymbol{\lambda}| > 0$ vanish (see Appendix D). As a consequence, a quantized amount of physical spin will be transported after each cycle, equal to the winding number of the map $\hat{\mathbf{d}}$ from the torus $\mathbb{T}^2$ to the 2-sphere. From a macroscopic perspective, the winding number manifests in the spin-dipole moment density that acquires nonzero values and winds once as a function of ϕ [see Fig. 3(b)]. Even though the spin current of our model has a simple analytic solution, we note that for more complicated band structures, numerical tools can be used to calculate the relevant quantities from first principles [55,124–127]. Interestingly, when $|\boldsymbol{\lambda}|$ is sufficiently large with respect to the spectral gap, a topological phase transition may occur as the spin-Chern number changes to zero.

2. Accumulation

Before focusing on the spinor degree of freedom, we briefly mention that the question of charge accumulation on a domain wall created by a spatially modulated 1D Hamiltonian has been previously studied in the context of high-energy physics in Ref. [101]. The system was shown to support a nontrivial solution, called a soliton, which is exponentially localized on the domain wall and results in a fractional charge accumulation of $1/2$. As we will see here, the fractional accumulation of charge, and more generally of a spinor degree of freedom, is related to the first spinor-Chern flux defined over the momentum-position coordinates of the system.

In order to observe nontrivial effects in spinor accumulation, the Hamiltonian is now modulated in position by introducing a spatial dependence in the external parameter $\phi(r)$, e.g., by changing the on-site energy and hopping terms in Eq. (16) over position space. Specifically, we assume that $\phi(r)$ acquires continuous values between zero and π [see Fig. 4(a)], with smooth enough modulations as compared to the size of the wave packet. In this regime, the curvature tensor of the local bands is given by $\Omega^{nm}_{rk} = i\partial_r\phi(\langle\partial_\phi n|\partial_k m\rangle - \langle\partial_k n|\partial_\phi m\rangle)$ and the induced spinor density at half filling [cf. Eq. (8)] by

$$\rho_{\hat{\mathcal{S}}} = -\frac{1}{2\pi} \int_{\mathbb{T}^1} dk \, \mathrm{Tr}\, \underline{\mathcal{S}} \Omega_{rk}, \tag{33}$$

where the integration of the momentum k is over the entire 1D Brillouin zone denoted by $\mathbb{T}^1$. The total spinor accumulation $q_{\hat{\mathcal{S}}}$ in a region C enclosing the domain wall is, thus, given by

$$q_{\hat{\mathcal{S}}} = \int_C dr \rho_{\hat{\mathcal{S}}} =: -\Phi_1, \tag{34}$$

where $\Phi_1 \sim \int_{\mathbb{T}^1\times[0,\pi]} dk d\phi \, \mathrm{Tr}\, \underline{\mathcal{S}}\Omega_{\phi k}$ is the first spinor-Chern flux attached to the 2D Dirac-like cones in the (k,ϕ) parameter space [cf. Fig. 2(b)]. We emphasize that Eq. (34) is valid for any insulating ground state and is not limited to Hamiltonian (22).

Within the classical approach of multipole moments, Eq. (34) can be alternatively described by the spatial gradient of a bulk spinor-dipole density, i.e., $q_{\hat{\mathcal{S}}} = -\int_C dr \partial_r \mathcal{P}^{\hat{\mathcal{S}}}$, where $\mathcal{P}^{\hat{\mathcal{S}}}$ is again the spinor-dipole moment density (cf. Appendix B) and C is the integration domain over space (related to an integration over ϕ by the appropriate coordinate transformation). Consequently, the first spinor-Chern flux Φ_1 is identified with the contribution from a spatially modulated spinor-dipole moment density, i.e.,

$$\Phi_1 \overset{!}{=} \int_C dr \partial_r \mathcal{P}^{\hat{\mathcal{S}}}. \tag{35}$$

Similar to the derivation of spinor transport, the above equation leads to a fundamental connection between an abstract geometrical quantity and an electronic property of the material.

In general, the integration domain C in Eq. (34) does not necessarily cover a closed manifold in the (k,ϕ) parameter space; therefore, Φ_1 is not expected to be quantized. However, under symmetry constraints the first spin-Chern flux of the tight-binding model of Eq. (22) can, in fact, become quantized and lead to a fractional spin accumulation localized at the domain wall. Specifically, the first spin-Chern flux correct up to first order in the spin-orbit interaction (cf. Appendix D) is given by

$$\Phi_1 = \frac{1}{4\pi}\int_{\mathbb{T}^1\times[0,\pi]} dk d\phi \, \hat{\mathbf{d}}\cdot(\partial_k\hat{\mathbf{d}}\wedge\partial_\phi\hat{\mathbf{d}}), \tag{36}$$

where $\mathbb{T}^1\times[0,\pi]$ represents the one-dimensional Brillouin zone $\mathbb{T}^1$ and the integration region $[0,\pi]$ in the ϕ parameter space. The integrand in the above equation is relatively featureless except around two isolated points $(k_0,\phi_0) = (\pi, \pm\pi/2)$, where the band gap becomes a minimum. The curvature around these points defines a two-dimensional monopole in the (k,ϕ) parameter space that carries a finite spin given in the linearized regime by

$$\frac{1}{\pi}\int_0^\Lambda d\delta k d\delta\phi \frac{h_0}{\left(\delta k^2+\delta\phi^2+h_0^2\right)^{3/2}} \overset{\frac{h_0}{\Lambda}\to 0^+}{=} \frac{1}{2}, \tag{37}$$

where Λ is a cutoff energy, and $\delta k = vk$ $(\delta\phi = u\phi)$ is the linearized momentum (external parameter) with $v = J$ $(u = -2\Delta J^0)$ the associated Fermi velocity. Importantly, in its chiral limit, i.e., when $h_0/\Lambda \to 0$, the expression for the first spin-Chern flux and, hence, the amount of spin that is supported on the domain wall become *quantized* and equal to $1/2$ [see Fig. 4(b)]. Indeed, the bulk spin-dipole moment of each spin sector changes by a fractional amount between $\phi = 0$ and π [cf. Fig. 3(a)], as a consequence of chiral symmetry χ. On the other hand, the electric dipole moment vanishes in the entire parameter space, as it is given by the sum of two equal but opposite contributions. The latter is also reflected in the trivial first Chern flux associated to the charge degree of freedom.

B. In two dimensions

In this section, we use the semiclassical theory to establish a connection between quantized spinor transport (accumulation) in 2D insulators and the spinor-Chern numbers (fluxes) characterizing the system's phase space. We illustrate this connection by calculating the spin current up to second order in the adiabatic driving of a concrete tight-binding model describing spinful electrons on a square lattice. In particular, we show that the transported spin after a pump cycle is proportional to not just the first sub-spin-Chern number (discussed in Sec. III A), but also to a second spin-Chern number defined over the four-dimensional parameter space of the system. Similarly, the spin density is related to the first and second spin-Chern fluxes that give rise to nonzero spin accumulation at the edges and corners, respectively. Finally, we decompose the spin transport and accumulation in terms of modulations of spin-multipole moments and propose a dynamical scenario where an adiabatically driven, weakly inhomogeneous 2D crystal exhibits a quantized spin transport and fractional spin accumulation with codimensions 2.

A tight-binding model that contains all necessary ingredients is shown in Fig. 5(a). It describes noninteracting spinful electrons on a 2D square lattice with Hamiltonian $H = H_{\mathrm{KE}} + H_{\mathrm{d}} + H_{\mathrm{h}} + H_{\mathrm{SO}}$. The first term is the kinetic energy, given by

$$H_{\mathrm{KE}} = \sum_{\boldsymbol{n},j,\alpha} J_j\left(e^{iA_j}c^\dagger_{\boldsymbol{n}+\hat{e}_j,\alpha}c_{\boldsymbol{n},\alpha} + \mathrm{H.c.}\right), \tag{38}$$

where indices $i \in \{x,y\}$ run over two directions, J_i is the hopping amplitude in the ith direction with unit vector $\hat{e}_i$, $\boldsymbol{n} = (n_x, n_y)$ is the position vector in the 2D lattice, α is the spin index, $\boldsymbol{A} = (0, -\pi n_x)$ is a static vector potential, and the lattice spacing is taken to be unity. The kinetic term describes hopping of electrons with spin α between neighboring sites on a square lattice with π-flux quanta per plaquette. Similar to the one-dimensional case of Eq. (16), the second term in H defines the dimerization of the hopping amplitudes in the two directions:

$$H_{\mathrm{d}} = \sum_{\boldsymbol{n},j,\alpha}(-1)^{n_j}\Delta J_j\left(e^{iA_j}c^\dagger_{\boldsymbol{n}+\hat{e}_j,\alpha}c_{\boldsymbol{n},\alpha} + \mathrm{H.c.}\right). \tag{39}$$

The next term is a checkerboard on-site potential $H_{\mathrm{h}} = h\sum_{\boldsymbol{n},\alpha,\beta}(-1)^{n_x+n_y}\tau^z_{\alpha\beta}c^\dagger_{\boldsymbol{n},\alpha}c_{\boldsymbol{n},\beta}$ that couples antiferromagnetically to the physical spin, while the last term is given by

$$H_{\mathrm{SO}} = \sum_{\boldsymbol{n},j,\alpha,\beta} i\boldsymbol{\lambda}^j\cdot\boldsymbol{\tau}_{\alpha\beta}e^{iA_j}\left(c^\dagger_{\boldsymbol{n}+\hat{e}_j,\alpha}c_{\boldsymbol{n},\beta} - c^\dagger_{\boldsymbol{n},\alpha}c_{\boldsymbol{n}+\hat{e}_j,\beta}\right), \tag{40}$$

where $\boldsymbol{\lambda}^i = \{\lambda^i_1, \lambda^i_2, \lambda^i_3\}$ is an arbitrary vector characterizing the spin-orbit interaction along the ith direction and it plays a role similar to Dzyaloshinskii-Moriya interaction.

Our tight-binding modeling is motivated by recent experiments in 2D magnetic $SrIrO_3$ and $SrTiO_3$ materials [128]

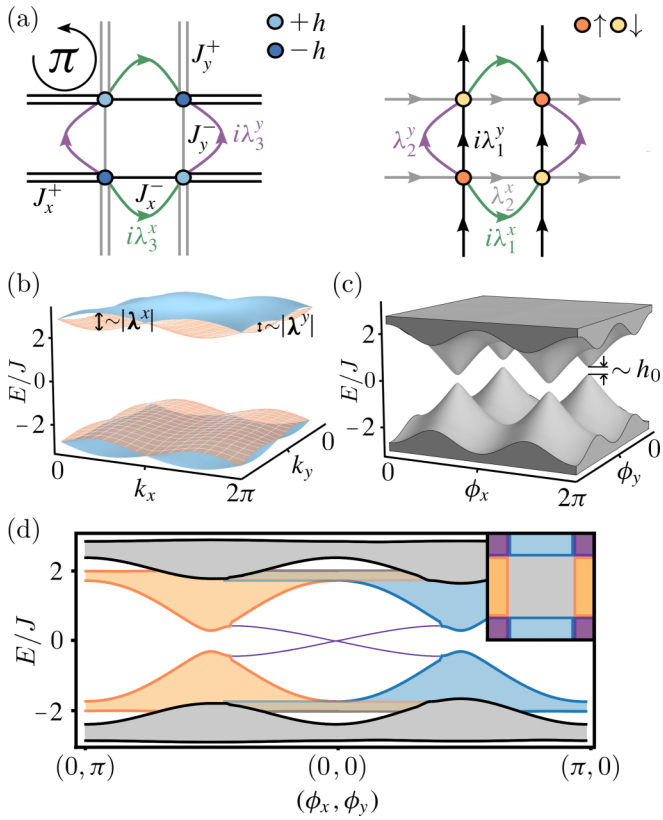

FIG. 5. The model Hamiltonian in two dimensions. (a) Left: The tight-binding lattice showing electrons with spin α tunneling to the nearest neighbor in the ith direction with amplitude $J_i^{\pm} = J_i \pm \Delta J_i$, denoted by single and double lines. The light (dark) blue sites denote an on-site potential with positive (negative) sign depending on α. The τ_z component of the spin-orbit interaction in the different directions is denoted by the green (purple) curved lines. The lattice is additionally threaded by a strong magnetic field of π-flux quanta per plaquette. Right: The tight-binding lattice describing hopping between spin-up and -down electrons, denoted by the yellow and orange sites, respectively. The τ_x (τ_y) component of the spin-orbit interaction in the different directions is denoted by the green (gray) and black (purple) lines. (b) The bulk spectrum of the Hamiltonian $H(\boldsymbol{k}, \boldsymbol{\phi})$ at $\boldsymbol{\phi} = (0, 0)$ showing four doubly degenerate bands. (c) The bulk spectrum as a function of the external parameters showing the four 4D Dirac-like crossings where the mass term is proportional to h_0. Each point in the $\boldsymbol{\phi}$ plane represents the bulk spectrum in the entire Brillouin zone $\boldsymbol{k}$, projected onto the perpendicular axis. (d) The open boundary spectrum of the Hamiltonian showing bulk (gray), edge (blue and orange), and corner (purple) states. The inset shows a schematic representation of the different states found in the open boundary spectrum. For all simulations we used $J_i/10 = J_i - \Delta J_i^0 = 0.1$. In (b) we used $\lambda_1^x/6 = \lambda_2^y/3 = 0.1$ to emphasize the effect of spin-orbit coupling in the different directions. In (c) and (d) we used $\lambda_1^x = \lambda_2^y = 0.1$ where the former has $h_0 = 0.1$ and the latter $h_0 = 0.5$. The remaining parameters are set to zero.

where a highly efficient control of the antiferromagnetic order was demonstrated using a uniform magnetic field. Alternative implementations may also be found in piezoelectric and piezomagnetic crystals, where electric and magnetic properties are controlled by lattice deformations. With these studies in mind, we assume that the dimerization parameter and on-site checkerboard potential depend on two external parameters $\boldsymbol{\phi} = (\phi_x, \phi_y)$,

$$\Delta J_i = \Delta J_i^0 \cos(\phi_i) \quad \text{and} \quad h = h_0 \prod_i \sin(\phi_i), \tag{41}$$

where the spatiotemporal variations of $\boldsymbol{\phi}$ are smooth enough such that the system can be expanded in terms of a local Hamiltonian and the semiclassical dynamics are well captured within second-order perturbation theory (cf. Sec. II).

The momentum-space Hamiltonian as a function of the external parameters $\boldsymbol{\phi}$ is given by

$$H(\boldsymbol{k}, \boldsymbol{\phi}) = \boldsymbol{d} \cdot \boldsymbol{\gamma} + \boldsymbol{D} \cdot \boldsymbol{\Gamma}, \tag{42}$$

where, now, $\boldsymbol{d}$ and $\boldsymbol{D}$ are 5- and 12-vectors, respectively,

$$\begin{aligned}
\boldsymbol{d} = \{&h, J_x^+ + J_x^- \cos(k_x), J_x^- \sin(k_x),\\
&J_y^+ + J_y^- \cos(k_y), J_y^- \sin(k_y)\},\\
\boldsymbol{D} = \big\{&\lambda_1^x \sin(k_x), -\lambda_1^x + \lambda_1^x \cos(k_x), \lambda_2^x \sin(k_x),\\
&-\lambda_2^x + \lambda_2^x \cos(k_x), \lambda_3^x \sin(k_x), -\lambda_3^x + \lambda_3^x \cos(k_x),\\
&\lambda_1^y \sin(k_y), -\lambda_1^y + \lambda_1^y \cos(k_y), \lambda_2^y \sin(k_y),\\
&-\lambda_2^y + \lambda_2^y \cos(k_y), \lambda_3^y \sin(k_y), -\lambda_3^y + \lambda_3^y \cos(k_y)\big\},
\end{aligned}$$

with $J_i^{\pm} = J_i \pm \Delta J_i$, and

$$\begin{aligned}
\boldsymbol{\gamma} = \{&\tau_z \otimes \sigma_z \otimes \mathbb{1}, \mathbb{1} \otimes \sigma_x \otimes \mathbb{1}, \mathbb{1} \otimes \sigma_y \otimes \sigma_z,\\
&\mathbb{1} \otimes \sigma_y \otimes \sigma_y, \mathbb{1} \otimes \sigma_y \otimes \sigma_x\}
\end{aligned}$$

are five 8×8 anticommuting Hermitian matrices $\{\gamma_\mu, \gamma_\nu\} = 2\delta_{\mu\nu}$. Finally, the spin-orbit interaction is represented by twelve 8×8 unitary matrices:

$$\begin{aligned}
\boldsymbol{\Gamma} = \{&\tau_x \otimes \sigma_x \otimes \mathbb{1}\,, \tau_x \otimes \sigma_y \otimes \sigma_z, \tau_y \otimes \sigma_x \otimes \mathbb{1},\\
&\tau_y \otimes \sigma_y \otimes \sigma_z, \tau_z \otimes \sigma_x \otimes \mathbb{1}\,, \tau_z \otimes \sigma_y \otimes \sigma_z,\\
&\tau_x \otimes \sigma_y \otimes \sigma_y, \tau_x \otimes \sigma_y \otimes \sigma_x, \tau_y \otimes \sigma_y \otimes \sigma_y,\\
&\tau_y \otimes \sigma_y \otimes \sigma_x, \tau_z \otimes \sigma_y \otimes \sigma_y, \tau_z \otimes \sigma_y \otimes \sigma_x\}.
\end{aligned}$$

The energy spectrum of Hamiltonian (42) has eight bands [see Fig. 5(b)]. Each set of positive- and negative-energy bands can be written as a direct sum of two orthogonal groups of eigenvectors that are coupled by the spin-orbit interaction. Each pair of groups remains degenerate in the entire Brillouin zone when the spin-orbit interaction vanishes, $\sum_i |\boldsymbol{\lambda}^i| = 0$; otherwise, the degeneracy survives only at isolated points. At half filling the system is conducting only when $\sum_i |\Delta J_i| = h = 0$, and insulating if either the staggered potential h or the dimerization parameters ΔJ_x or ΔJ_y become nonzero [see Fig. 5(c)].

Introducing open boundary conditions and solving for the eigenenergies, we find that in addition to the bulk bands, the spectrum has two sets of codimension-1 (edge) states: (i) right and left localized states and (ii) top and bottom localized states [see Fig. 5(d)]. As a function of $\boldsymbol{\phi}$, the edge states disperse and merge into the bulk bands without crossing the gap. Each set of right and left or top and bottom states is localized in opposite sites of the crystal; hence, their sum vanishes when calculating the charge polarization of the ground state at half filling. Similarly, the spin-density distribution of edge states has vanishing contribution to the total spin polarization.

The spectrum supports an additional set of codimension-2 states localized at the corners. In contrast to the codimension-1 states, as a function of $\boldsymbol{\phi}$ the corner states disperse, merge with edge or bulk states, and most importantly cross the gap. However, such spectral flow does not induce any net charge transport since the states that cross the gap are made up of two electrons and two holes; on the other hand, a heat and spin transport is expected to show nontrivial effects.

Hamiltonian (42) has TR symmetry $\Theta = i\mathbb{K}\tau_y \otimes \mathbb{1} \otimes \mathbb{1}$ and chiral symmetry $\chi = \mathbb{1} \otimes \sigma_z \otimes \mathbb{1}$ for any value of ΔJ_i and $\boldsymbol{\lambda}^i$, only when $h = 0$. Additionally, the Hamiltonian has charge conjugation symmetry $C = i\mathbb{K}\tau_y \otimes \sigma_z \otimes \mathbb{1}$ in the entire phase space; i.e.,

$$C^{-1}H(\boldsymbol{k}, \boldsymbol{\phi})C = -H(-\boldsymbol{k}, -\boldsymbol{\phi}), \tag{43}$$

for any value of ΔJ_i, $\boldsymbol{\lambda}^i$, and h. Hence, the occupied subspace of Bloch states can be partitioned into conjugate partners with a characteristic 4D Z_2 index [13]. As we show below, this index emerges in the second-order corrections to the spin transport and accumulation that is induced by spatiotemporal modulations of the crystal.

Since the dimensionality of phase space can now support a variety of nontrivial curvatures, here we summarize their physical origins. As discussed in Sec. III A, adiabatic drives give rise to mixed momentum-time curvatures $\Omega_{k_i t}$, while weak inhomogeneities give rise to momentum-position curvatures $\Omega_{k_i r_j}$. Any weak external magnetic field that threads the insulator is incorporated via the position curvature $\Omega_{r_i r_j} \equiv B_{ji}$, and electric fields via the mixed position-time curvature $\Omega_{t r_i} \equiv E_i$. Finally, a momentum curvature $\Omega_{k_i k_j}$ arises as the relevant geometrical quantity in momentum space.

1. Transport

The topological corrections to electronic charge transport up to second order have been extensively studied using the semiclassical theory [70,73,74,129–132]. At first order, Hall currents were shown to be related to a first Chern number in momentum space, while second-order effects gave rise to 2D topological charge pumps with a second Chern number response. The relation of these indices to robust boundary physics, namely, to codimension-1 and -2 states, has been demonstrated in cold atomic clouds [21–26], photonic lattices [27–32], metamaterials [33–40], and electrical circuits [41–46]. Here, we extend this description to spinor degrees and derive the spinor-Hall effect, as well as 2D topological spinor pumps. Specifically, we show how a first and second spinor-Chern number manifest as corrections to the spinor current and highlight the relation to the quantized changes of spinor-multipole moments.

The semiclassical equations of motion (2) valid up to second order in perturbation theory result in a nonvanishing spinor current [70],

$$j^i_{\hat{\mathcal{S}}} = \int_{\mathbb{T}^2} \frac{d^2k}{(2\pi)^2} \operatorname{Tr} \underline{S}\left(\Omega_{t k_i} - \epsilon^{ij}\epsilon^{lm}\Omega_{t k_l}\Omega_{r_j k_m} + \epsilon^{ij}\Omega_{k_x k_y}E_j\right), \tag{44}$$

where the mixed time-position curvature is replaced by the electric field $\Omega_{t r_i} \equiv E_i$, the integration domain is over a $\mathbb{T}^2$-torus representing the 2D Brillouin zone, $\epsilon^{xy} = 1$ is the two-dimensional Levi-Cività tensor, and $\underline{S}$ is the matrix representation of the spinor operator in the basis of occupied states. The spinor current has contributions from (i) a curvature in (t, k_i) coordinate space representing the adiabatic drive of the ΔJ_i dimerization parameter, (ii) a product of curvatures in the $(\boldsymbol{r}, \boldsymbol{k}, t)$ coordinate space from the simultaneous drive and deformation of the crystal, and (iii) a combination of momentum curvature and applied electric field. When $\hat{\mathcal{S}}$ represents the charge degree, the latter is reduced to the usual quantum Hall response where the current depends on the first Chern number in momentum space, $c_1 \sim \int_{\mathbb{T}^2} d^2k \Omega_{k_x k_y}$. Analogously, when $\hat{\mathcal{S}}$ is the spin degree we obtain the quantum spin-Hall effect with a spin-current response proportional to a $\mathbb{Z}_2$ topological index $c_1 \sim \int_{\mathbb{T}^2} d^2k \tau_z \Omega_{k_x k_y}$. As these Hall effects are well established, we omit them for the remaining calculations.

The transport of spinor charges in the ith direction after a pump cycle $t \in [t_0, t_0 + T]$ is given by

$$\Delta q^i_{\hat{\mathcal{S}}} = \int_{T,V} dt d^2r \, j^i_{\hat{\mathcal{S}}} = c^i_1 - c^i_2, \tag{45}$$

where the integral runs over a period T and the volume of the unit cell, $V \in [0, l_x] \times [0, l_y]$, is hereafter taken to be unity for simplicity. Remarkably, we find that the perturbative corrections to the spinor transport are proportional to topological quantities defined in the system's phase space. Namely, at first order we find a first sub-spinor-Chern number c^i_1, defined as

$$c^i_1 = \frac{1}{(2\pi)^2} \int_{T,V,\mathbb{T}^2} dt d^2r d^2k \operatorname{Tr} \underline{S} \Omega_{t k_i}. \tag{46}$$

At second order, a second spinor-Chern number arises, defined as

$$c^i_2 = \frac{1}{(2\pi)^2} \int_{T,V,\mathbb{T}^2} dt d^2r d^2k \epsilon^{ij}\epsilon^{lm} \operatorname{Tr} \underline{S} \Omega_{t k_l} \Omega_{r_j k_m}. \tag{47}$$

The above equation indeed defines the set of second spinor-Chern numbers that characterize the momentum-position-time coordinate space [cf. Eq. (11)] since terms proportional to $\Omega_{t r_j}$ will vanish in the absence of external electromagnetic field perturbations.

Extending the electric polarization in macroscopic materials to higher spinor-multipole moments, we decompose the bulk spinor current as

$$j^i_{\hat{\mathcal{S}}} = \partial_t \mathcal{P}^{\hat{\mathcal{S}}}_i - \partial_t \partial_{r_j} \mathcal{Q}^{\hat{\mathcal{S}}}_{ij}, \tag{48}$$

where $\boldsymbol{\mathcal{P}}^{\hat{\mathcal{S}}}$ is the spinor-dipole moment density vector, and $\mathcal{Q}^{\hat{\mathcal{S}}}_{ij}$ is the spinor-quadrupole moment density in position space (cf. Appendix B). Equations (44) and (48) establish a fundamental connection between topological quantities defined in the system's phase space and the modulations of the spinor-dipole and spinor-quadrupole moment densities, namely,

$$c^i_1 - c^i_2 \overset{!}{=} \int_{T,V} dt d^2r \left(\partial_t \mathcal{P}^{\hat{\mathcal{S}}}{}_i - \partial_t \partial_{r_j} \mathcal{Q}^{\hat{\mathcal{S}}}_{ij}\right). \tag{49}$$

We emphasize that the above equation is independent of the particular Hamiltonian and can be used as a general geometrical definition of the spinor-multipole moments in two dimensions—a definition that eliminates any gauge ambiguity, as it is based on integrated differences.

Focusing on our specific tight-binding model of Eq. (42), nontrivial spinor currents can be induced by adiabatically driving and periodically modulating in space the external parameters $\boldsymbol{\phi}$. For simplicity, we assume $\dot{\phi}_x = 2\pi/T$ and $\partial_x \phi_y = 2\pi/l$ with T (l) the period (length scale) of the modulation. The proper static deformation of the internal parameters is a crucial ingredient in 2D topological pumps as without it the second spinor-Chern number becomes trivial (see, for example, Ref. [49]). By defining $\hat{\mathcal{S}} = \mathbb{1} \otimes \mathbb{1} \otimes \mathbb{1}$ (or $\tau_z \otimes \mathbb{1} \otimes \mathbb{1}$) as the charge (spin) operator, we calculate the first sub-spinor-Chern numbers and find that they identically vanish for both the charge and spin degree of freedom, i.e., $c_1^i = 0$ for all i. Additionally, the second Chern number associated to the charge degree of freedom is zero because of the anticommuting and traceless properties of the $\boldsymbol{\gamma}$ matrices. On the other hand, the second spin-Chern number associated with physical spin $\hat{S} = \tau_z \otimes \mathbb{1} \otimes \mathbb{1}$ becomes nontrivial and equal to

$$c_2^i = \frac{3}{8\pi^2} \int_{\mathbb{T}^4} d^2k d^2\phi \, \delta_{iy} \times \hat{\mathbf{d}} \cdot \left(\partial_{k_x} \hat{\mathbf{d}} \wedge \partial_{k_y} \hat{\mathbf{d}} \wedge \partial_{\phi_x} \hat{\mathbf{d}} \wedge \partial_{\phi_y} \hat{\mathbf{d}}\right), \tag{50}$$

where $\hat{\boldsymbol{d}} = \boldsymbol{d}/|\boldsymbol{d}|$, and δ_{ij} is the Dirac delta function. The latter is a consequence of the chosen driving scheme and stems from the Jacobian transformation $\dot{\phi}_i \partial_{r_x} \phi_j = (2\pi)^2 \delta_{ix} \delta_{jy}$ between phase-space coordinates $\boldsymbol{\xi}$ and the parameter space $(\boldsymbol{k}, \boldsymbol{\phi})$. Since a nonzero spin-orbit interaction has vanishing first-order contributions to Eq. (50) (see Appendix D), the spin transport along the y direction is an integer determined by the winding number of the map $\hat{\mathbf{d}}$ from $\mathbb{T}^4$ to the 4-sphere. Hence, spin transport can be readily understood in the framework of a 4D $\mathbb{Z}_2$ insulator where the top topological invariant is given by the difference of the "mirror" second Chern numbers characterizing the eigenstates from the two spin sectors.

The relation between spin transport, the second spin-Chern number, and the spin-quadrupole moment is illustrated in Fig. 6(a). First, we note that the calculated electric and spin-dipole moments vanish in the entire phase space, reflecting the trivial values of the first spinor-Chern numbers. Similarly, the electric quadrupole moment is decomposed into two equivalent contributions that originate from the two occupied (doubly degenerate) spin sectors. As these contributions come with opposite signs, the net electric quadrupole moment is zero in the entire parameter space; correspondingly, the second Chern number associated to the charge degree of freedom is zero. On the contrary, the spin-quadrupole moment of the model becomes nonzero and, in fact, "winds" twice as a function of the external parameters $\boldsymbol{\phi}$. This higher-dimensional winding manifests as a nontrivial second spin-Chern number, given by Eq. (50), and to a quantized spin transport, equal to 2.

2. Accumulation

In a two-dimensional system there are two kinds of boundary states that can appear: with codimensions 1 or 2. The former corresponds to states localized in one direction but extended in the other, found, for example, on the edges of Hall systems or in insulators with nonzero intrinsic polarization. On the other hand, the interesting properties of codimension-2 states have only recently been rigorously explored. This led to the prediction and observation of states which are localized in both dimensions and, under certain symmetry constraints, carry a quantized charge $\pm 1/2$ [15,32,33,43,51–58,60–62,67]. From these studies, a new class of TIs emerged, dubbed "higher-order TIs," where a d-dimensional insulator has nontrivial boundary phenomena manifesting at its d-h boundary, where $h \geqslant 1$. The associated electric multipole moments of higher-order TIs can be readily calculated using the modern theory of Wilson, and nested Wilson loops [55]. For codimension-2 states, the key observable is the quadrupole moment which is constrained to obtain only certain values and, as a result, quantize the accumulation of electronic charge at the corner.

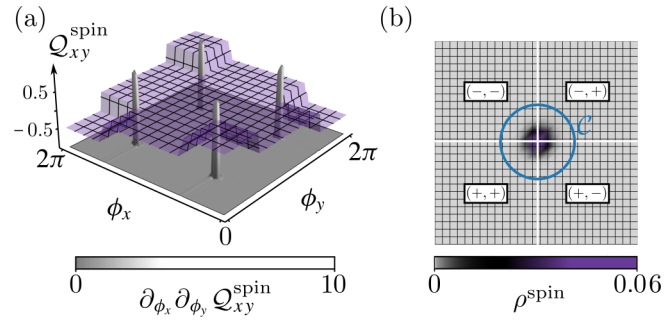

FIG. 6. Spin observables in the chiral limit. (a) The spin quadrupole moment (cf. Appendix B) "winds" twice in the two-dimensional parameter space $\boldsymbol{\phi}$. This is in correspondence with the four singular contributions to the second spin-Chern number where each integrates to 1/2 [cf. Eq. (55)]. (b) The spin density of the electronic ground state at half filling. The $\pm$ sign shown in the four quadrants indicates the values of $\boldsymbol{\phi}$ (zero or π, respectively) and creates a domain wall that supports a nonzero spin density. The total amount of spin in region $\mathcal{C}$ is quantized and equal to 1/2. For the simulations we used $J_i/10 = J_i - \Delta J_i^0 = 0.1$, $|\boldsymbol{\lambda}^i| = \lambda_1^i = 0.1$ (for both $i = x$ and y), and $h_0 = 0.001$. The remaining parameters are set to zero.

As we will see in this section, an alternative definition of second-order TIs and its extension to what we dub "spinor-second-order TIs" is naturally obtained within the semiclassical theory. Specifically, we show that geometrical properties of phase space—the spinor-Chern fluxes—appear as corrections to the spinor density, directly leading to a fractional accumulation at the zero-dimensional (0D) or 1D boundaries when symmetry constraints are imposed. Finally, we show how these quantities are related to the spinor-multipole moments, namely, the spinor-dipole and spinor-quadrupole moment.

In general, a weakly inhomogeneous insulator under electromagnetic fields in two spatial dimensions is well characterized by the spinor density up to second-order corrections [cf. Eq. (8)]:

$$\rho_{\hat{\mathcal{S}}} = \int_{\mathbb{T}^2} \frac{d^2k}{(2\pi)^2} \operatorname{Tr} \underline{S} \left(- \sum_i \Omega_{r_i k_i} + \frac{1}{2} \epsilon^{ij} \epsilon^{lm} \Omega_{k_i r_l} \Omega_{k_j r_m} + \Omega_{k_x k_y} B_{xy} \right), \tag{51}$$

where the position curvature is replaced by the magnetic field $\Omega_{r_i r_j} \equiv B_{ji}$. When considering the charge degree of freedom, the last term corresponds to the Streda formula [6] that relates the change of the density of states induced by an applied magnetic field to the first Chern number in momentum space, i.e., $\partial_{B_{xy}} \rho_{\text{charge}} = c_1$. Since such corrections uniformly shift the spinor density by a constant, hereafter these are omitted for simplicity. The remaining terms in Eq. (51) are proportional to the momentum-position curvatures and become nontrivial when deformation fields are applied.

Calculating the total spinor charge in an arbitrary region $\mathcal{C}$ in position space we find

$$q_{\hat{\mathcal{S}}} = \int_{\mathcal{C}} d^2 r \rho_{\hat{\mathcal{S}}} = -\sum_i \Phi_1^i + \Phi_2. \tag{52}$$

The first term corresponds to geometrical contributions from a set of first spinor-Chern fluxes Φ_1^i, defined over the respective (r_i, k_i) submanifold [cf. Eq. (13)],

$$\Phi_1^i = \frac{1}{(2\pi)^2} \int_{\mathcal{C},\mathbb{T}^2} d^2 r d^2 k \, \mathrm{Tr}\, \underline{S} \Omega_{r_i k_i}. \tag{53}$$

In similitude to the one-dimensional case [cf. Eq. (34)], these terms give rise to spinor accumulation with codimensions 1 and can be generally quantized by global symmetry constraints. An interesting manifestation of the above first spinor-Chern number in two dimensions are the helical edge states that appear at the boundaries of the insulator [133,134].

In addition to the first spinor-Chern fluxes, at second order in the inhomogeneities we find a new geometrical contribution proportional to the second spinor-Chern flux Φ_2 defined in the entire position-momentum space $(\boldsymbol{r}, \boldsymbol{k})$ [cf. Eq. (14)],

$$\Phi_2 = \frac{1}{(2\pi)^2} \int_{\mathcal{C},\mathbb{T}^2} d^2 r d^2 k \, \frac{1}{2} \epsilon^{ij} \epsilon^{lm} \, \mathrm{Tr}\, \underline{S} \Omega_{k_i r_l} \Omega_{k_j r_m}. \tag{54}$$

Importantly, this quantity is intrinsically four dimensional and vanishes for manifolds with dimensions 3 or less. Since the integration region $\mathcal{C}$ is an open domain in position space, Φ_2 is generally not expected to be quantized. However, as we show below, under symmetry constraints it can become quantized and fractional.

The nontrivial effects of the spinor-Chern fluxes manifest in the 2D model Hamiltonian of Eq. (42) when the external parameters $\boldsymbol{\phi}$ depend on space. Specifically, we assume ϕ_x (ϕ_y) is only a function of r_x (r_y) and takes continuous values between zero and π. The integration domain $\mathcal{C}$ is assumed to cover the intersection of the two domain walls [see Fig 6(b)]. In this case, the induced spinor density has vanishing contributions from the first spinor-Chern flux (both for charge and physical spin), as well as from the second Chern flux associated to the charge degree.

In contrast, the second spin-Chern flux associated to $\hat{\mathcal{S}} = \tau_z \otimes \mathbb{1} \otimes \mathbb{1}$ is nonzero and has a closed analytic form:

$$\frac{3}{8\pi^2} \int_{\mathbb{T}^2 \times [0,\pi]^2} d^2 k d^2 \phi \hat{\mathbf{d}} \cdot \left(\partial_{\mathrm{k}_x} \hat{\mathbf{d}} \wedge \partial_{\mathrm{k}_y} \hat{\mathbf{d}} \wedge \partial_{\phi_x} \hat{\mathbf{d}} \wedge \partial_{\phi_y} \hat{\mathbf{d}} \right),$$

where $\mathbb{T}^2 \times [0,\pi]^2$ is the integration domain in the four-dimensional parameter space $(\boldsymbol{k}, \boldsymbol{\phi})$, and we have used the Jacobian transformation $\partial_{r_x} \phi_i \partial_{r_y} \phi_j = (2\pi)^2 \delta_{ix} \delta_{jy}$ between position coordinates $\boldsymbol{r}$ and the external parameters $\boldsymbol{\phi}$. The above integral is determined by the covering of the map $\hat{\mathbf{d}}$ from the parameter space $(\boldsymbol{k}, \boldsymbol{\phi})$ to the 4-sphere. Similar to its lower-dimensional cousin of Eq. (37), it can be analytically calculated in the linearized regime around the isolated points $(\boldsymbol{k}_0, \boldsymbol{\phi}_0) = (\pi, \pi, \pm\pi/2, \pm\pi/2)$ as

$$\frac{6}{\pi^2} \int_0^\Lambda d^2 \delta k d^2 \delta \phi \frac{h_0}{\left(|\delta \boldsymbol{k}|^2 + |\delta \boldsymbol{\phi}|^2 + h_0^2 \right)^{5/2}} \overset{\frac{h_0}{\Lambda} \to 0^+}{=} \frac{1}{2}, \tag{55}$$

where $\delta \boldsymbol{k} = (v_x k_x, v_y k_y)$ and $\delta \boldsymbol{\phi} = (u_x \phi_x, u_y \phi_y)$ are the linearized vectors with $v_i = J_i$ ($u_i = -2\Delta J_i^0$) the Fermi velocity along the k_i (ϕ_i) coordinate, and Λ is the cutoff energy. When chiral symmetry is restored, i.e., when $h_0/\Lambda \to 0$, the second spin-Chern flux and, hence, the accumulated spin [cf. Eq. (52)] become fractional and equal to

$$|q_{\text{spin}}| = \tfrac{1}{2}.$$

The above equation is the extension of the fractional Berry flux attached to a 2D Dirac cone [cf. Eq. (37)], to the second spin-Chern flux of the 4D Dirac-like cone supported in the $(\boldsymbol{k}, \boldsymbol{\phi})$ parameter space [cf. Fig. 5(c)]. We note that first-order corrections to the second spin-Chern flux due to a nonzero spin-orbit interaction will vanish (see Appendix D).

Comparing with the classical expectation of the multipole description of materials, the calculated spinor density of Eq. (51) must be created by the spatial gradients of the spinor-multipole moments:

$$\rho_{\hat{\mathcal{S}}} = -\partial_{r_i} \mathcal{P}_i^{\hat{\mathcal{S}}} + \tfrac{1}{2} \partial_{r_i} \partial_{r_j} \mathcal{Q}_{ij}^{\hat{\mathcal{S}}}, \tag{56}$$

where repeating indices are summed. The multipole expansion of spinor density allows for a geometrical interpretation in terms of the first and second spinor-Chern fluxes, namely,

$$-\sum_i \Phi_1^i + \Phi_2 \overset{!}{=} \int_{\mathcal{C}} d^2 r \left(-\partial_{r_i} \mathcal{P}_i^{\hat{\mathcal{S}}} + \frac{1}{2} \partial_i \partial_j \mathcal{Q}_{ij}^{\hat{\mathcal{S}}} \right). \tag{57}$$

The connection between spinor-Chern fluxes defined over the phase space of the system and the accumulation of spinor charges is one of the main results of this paper: it connects an abstract geometrical property of phase space—the spinor-Chern fluxes—to physical observables—the modulations of spinor-multipole moments. Even though in general the latter lack a geometrical definition, the semiclassical formalism provides a well-defined way to connect integrated differences of the multipole moments to the geometrical properties of the system's phase space.

For the Hamiltonian model of Eq. (42), the spin-quadrupole moment takes nontrivial values in the parameter space $\boldsymbol{\phi}$ [see Fig. 6(a)]. When the spectral gap is minimum, the second gradient of the spin quadrupole with respect to $\boldsymbol{\phi}$ becomes nonzero, leading to a finite spin accumulation on the 2D domain wall shown in Fig. 6(b). In the limit where chiral symmetry χ is restored, the contributions from the spin-quadrupole moment become quantized and equal to $1/2$, as given by the second spin-Chern flux of Eq. (55). We note that the contributions from the spin-dipole moments evaluate to zero since these are related to trivial first spin-Chern fluxes. Similarly, the electric dipole and quadrupole moments vanish, as these are related to trivial first and second Chern fluxes, respectively. Even though for our particular model the

correspondence between spinor-Chern fluxes and changes of spinor-multipoles can be made one to one, we remark that, in general, Eq. (57) should be taken as a whole since a second spinor-Chern flux can additionally contribute to the change of the spinor-dipole moment [77].

C. In three dimensions

In this section, we generalize the concepts developed thus far to three-dimensional crystalline insulators. Specifically, we calculate the response of a 3D material under spatiotemporal modulations and general external electromagnetic fields using a semiclassical approach valid up to third order in perturbation theory. First, we derive the spinor analogs of the Hall effect and Streda formula in three dimensions, alongside nontrivial spinor-axion field responses in transport and accumulation. Next, we find that the spinor current has a unique third spinor-Chern number response associated to a topological index defined in the entire phase space, in addition to the first and second sub-spinor-Chern number responses encountered in Secs. III A and III B. Similarly, the spinor accumulation is shown to have contributions from the first, second, and third spinor-Chern fluxes that are associated to codimension-1, -2, and -3 states, respectively. Under symmetry constraints, we show that the spinor-Chern fluxes can become quantized, leading to a fractional spinor accumulation localized at the boundaries of the three-dimensional material. The spinor-Chern numbers and fluxes are ultimately related to the spatiotemporal modulations of the spinor-multipole moments.

These concepts are illustrated in the spin responses of a concrete tight-binding model of spinful electrons on a cubic lattice. Similar to the lower-dimensional analogs discussed in Secs. III A and III B, the key ingredients in the Hamiltonian are the nearest-neighbor interaction, the dimerization of the hopping amplitudes in the three directions, the staggered on-site potential, and the spin-orbit coupling. To keep the description less cumbersome, we directly use the momentum-space Hamiltonian [for an illustration of the real-space crystal, see Fig. 7(a)]

$$H(\boldsymbol{k},\boldsymbol{\phi}) = \boldsymbol{d}\cdot\boldsymbol{\gamma} + \boldsymbol{D}\cdot\boldsymbol{\Gamma}. \tag{58}$$

Here, $\boldsymbol{d}$ and $\boldsymbol{D}$ represent a 7- and an 18-component vector, respectively, with components

$$\boldsymbol{d} = \{h, J_x^+ + J_x^- \cos(k_x), J_x^- \sin(k_x), \ldots\},$$

where $J_i^\pm = J_i \pm \Delta J_i$, and

$$\boldsymbol{D} = \big\{\lambda_1^x \sin(k_x), -\lambda_1^x + \lambda_1^x \cos(k_x), \lambda_2^x \sin(k_x), \\ -\lambda_2^x + \lambda_2^x \cos(k_x), \lambda_3^x \sin(k_x), -\lambda_3^x + \lambda_3^x \cos(k_x), \ldots\big\},$$

where "…" denotes the remaining components in the y and z directions. The corresponding matrices are given by

$$\begin{aligned}\boldsymbol{\gamma} = \{&\tau_z\otimes\sigma_z\otimes\mathbb{1}\otimes\mathbb{1}, \mathbb{1}\otimes\sigma_x\otimes\mathbb{1}\otimes\sigma_x,\\ &\mathbb{1}\otimes\sigma_x\otimes\mathbb{1}\otimes\sigma_y, \mathbb{1}\otimes\sigma_x\otimes\mathbb{1}\otimes\sigma_z,\\ &\mathbb{1}\otimes\sigma_y\otimes\sigma_z\otimes\mathbb{1}, \mathbb{1}\otimes\sigma_y\otimes\sigma_y\otimes\mathbb{1},\\ &\mathbb{1}\otimes\sigma_y\otimes\sigma_x\otimes\mathbb{1}\},\end{aligned} \tag{59}$$

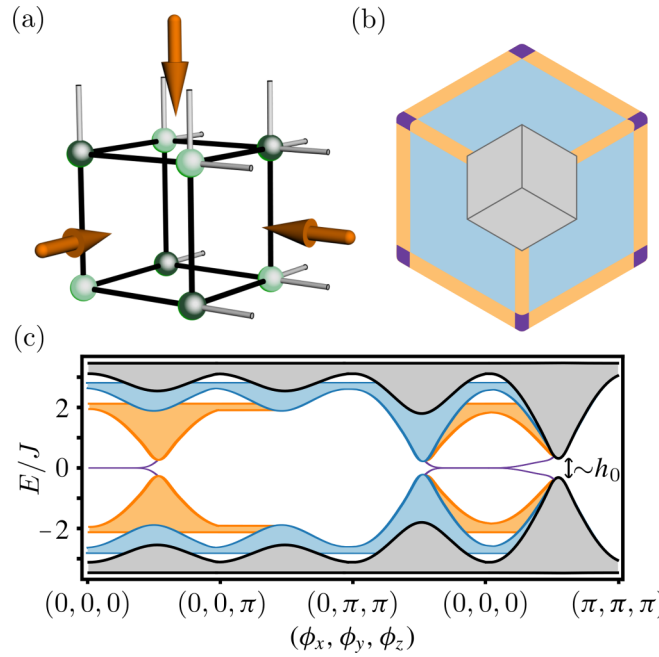

FIG. 7. The model Hamiltonian in three dimensions. (a) The 3D tight-binding lattice described by the Hamiltonian of Eq. (58). For simplicity, we only show hopping between equivalent spins. Light (dark) green sites denote an on-site potential with positive (negative) sign. Black (gray) lines denote hopping with amplitude J_i^+ (J_i^-). Each face of the cubic lattice is threaded by a strong magnetic field of π-flux quanta per plaquette. (b) The eigenstates of the open boundary spectrum are generally split into bulk (gray), surface (blue), hinge (orange), and corner (purple) states. (c) The open boundary spectrum of the Hamiltonian showing bulk (gray), surface (blue), edge (orange), and corner (purple) states. For the simulations we used $J_i/10 = \Delta J_i^0 = 0.1$, $h_0 = 0.25$, and $\sum_i |\boldsymbol{\lambda}^i| = 0$.

that define the kinetic and potential energy, as well as by the 18 matrices representing the spin-orbit interaction,

$$\begin{aligned}\boldsymbol{\Gamma} = \{&\tau_x\otimes\sigma_x\otimes\mathbb{1}\otimes\sigma_x, \tau_x\otimes\sigma_x\otimes\mathbb{1}\otimes\sigma_y,\\ &\tau_y\otimes\sigma_x\otimes\mathbb{1}\otimes\sigma_x, \tau_y\otimes\sigma_x\otimes\mathbb{1}\otimes\sigma_y,\\ &\tau_z\otimes\sigma_x\otimes\mathbb{1}\otimes\sigma_x, \tau_z\otimes\sigma_x\otimes\mathbb{1}\otimes\sigma_y,\\ &\tau_x\otimes\sigma_x\otimes\mathbb{1}\otimes\sigma_z, \tau_x\otimes\sigma_y\otimes\sigma_z\otimes\mathbb{1},\\ &\tau_y\otimes\sigma_x\otimes\mathbb{1}\otimes\sigma_z, \tau_y\otimes\sigma_y\otimes\sigma_z\otimes\mathbb{1},\\ &\tau_z\otimes\sigma_x\otimes\mathbb{1}\otimes\sigma_z, \tau_z\otimes\sigma_y\otimes\sigma_z\otimes\mathbb{1},\\ &\tau_x\otimes\sigma_y\otimes\sigma_y\otimes\mathbb{1}, \tau_x\otimes\sigma_y\otimes\sigma_x\otimes\mathbb{1},\\ &\tau_y\otimes\sigma_y\otimes\sigma_y\otimes\mathbb{1}, \tau_y\otimes\sigma_y\otimes\sigma_x\otimes\mathbb{1},\\ &\tau_z\otimes\sigma_y\otimes\sigma_y\otimes\mathbb{1}, \tau_z\otimes\sigma_y\otimes\sigma_x\otimes\mathbb{1}\}.\end{aligned} \tag{60}$$

We further assume that $H(\boldsymbol{k},\boldsymbol{\phi})$ describes a material where the dimerization parameters and on-site potential can depend on both space and time. Formally, this is implemented by a set of external parameters $\boldsymbol{\phi} = (\phi_x, \phi_y, \phi_z)$, where

$$\Delta J_i = \Delta J_i^0 \cos(\phi_i) \quad \text{and} \quad h = h_0 \prod_i \sin(\phi_i), \tag{61}$$

with ΔJ_i^0 and h_0 constants. The spatiotemporal modulations of $\boldsymbol{\phi}$ are assumed to be weak enough such that the wave

packet's equations of motion are well captured by third-order corrections (cf. Sec. II).

The bulk spectrum of the Hamiltonian is composed by 16 bands which are split into two sets of positive and negative energies. Each set can be further split into two quadruplets which are mixed depending on the spin-orbit interaction. When $\sum_i |\boldsymbol{\lambda}^i| = 0$, all positive (similarly, negative) energy states become degenerate, while this is lifted to isolated regions in the Brillouin zone when $\sum_i |\boldsymbol{\lambda}^i| > 0$. The material at half filling is conducting only when $\sum_i |\Delta J_i| = h = 0$.

The open boundary spectrum of the Hamiltonian has four distinct sets of states classified depending on their codimensionality [see Figs. 7(b) and 7(c)]. First are the dimension-0 states, i.e., bulk modes, which correspond to fully delocalized wavefunctions that have nonzero probability on lattice points deep within the bulk of the material; these correspond to the solutions of the Bloch Hamiltonian of Eq. (58). Next are the codimension-1 states that are localized in one of the coordinates but extended in the remaining two; these states are found on the surfaces of the 3D material. Then are the codimension-2 states, which are localized in two dimensions but extended in the third, e.g., spin-helix hinge states. Finally are codimension-3 states associated to fully localized states; such states appear on the corners of the material. As a function of the external parameters $\boldsymbol{\phi}$, the boundary states disperse, merge into other bands, and reemerge according to the lattice parameters; however, only the codimension-3 states cross the gap.

To conclude the description of the model, we note that the Hamiltonian has chiral symmetry $\chi = \mathbb{1} \otimes \sigma_z \otimes \mathbb{1} \otimes \mathbb{1}$ and TR symmetry $\Theta = i\mathbb{K}\tau_y \otimes \mathbb{1} \otimes \mathbb{1} \otimes \mathbb{1}$ only when $h = 0$. On the other hand, the parameter space has a global TR symmetry T for any value of ΔJ_i, $\boldsymbol{\lambda}^i$, and h.

1. Transport

Having seen the relation between spinor transport in weakly perturbed materials and spinor-Chern numbers in dimensions 1 and 2 (cf. Secs. III A 1 and III B 1), we now discuss topological transport in three dimensions and how it relates to the spinor-Chern numbers. Extending previous results for the charge degree [50], we show how the adiabatic evolution of the Hamiltonian induces a third-order correction proportional to the third spinor-Chern number. Alongside this unique response, we find a set of lower-dimensional indices, the first and second sub-spinor-Chern numbers, that appear as first- and second-order corrections to the spinor current. Additionally, by including nonzero external electromagnetic fields we derive the 3D spinor-Hall effect, as well as axion field responses in the spinor degrees of freedom. Finally, we show how our results manifest in the modulations of the spinor-multipole moments.

Using the semiclassical theory developed in Sec. II, a three-dimensional insulator in the absence of external electromagnetic fields is characterized by the spinor current

$$j^i_{\hat{\mathcal{S}}} = \int_{\mathbb{T}^3} \frac{d^3k}{(2\pi)^3} \operatorname{Tr} \underline{\mathcal{S}} \Big(\Omega_{tk_i} - \epsilon^{ijk}\epsilon^{klm}\Omega_{tk_l}\Omega_{r_jk_m} + \frac{1}{2}\epsilon^{ijk}\epsilon^{lmn}\Omega_{tk_l}\Omega_{r_jk_m}\Omega_{r_kk_n} \Big), \tag{62}$$

where the integration domain is over a $\mathbb{T}^3$-torus representing the 3D Brillouin zone, $\epsilon^{xyz} = 1$ is the three-dimensional Levi-Cività tensor, and Latin indices run over three directions $i \in \{x, y, z\}$. Depending on the particular Hamiltonian, the derived spinor current of Eq. (62) includes a variety of phenomena. The first term is equivalent to Eq. (28) and results in spinor transport proportional to a first sub-spinor-Chern number defined in the (t, k_i) manifold. The next term is a double product of curvatures and gives rise to 2D topological spinor pumps with a second sub-spinor-Chern number response [cf. Eq. (44)]. Finally, the last term is a unique three-dimensional response given by a triple product of curvatures in the entire $(\boldsymbol{r}, \boldsymbol{k}, t)$ phase space.

Next, when nonzero external electromagnetic fields are applied, we derive two additional corrections to Eq. (62). At first order we obtain

$$\int_{\mathbb{T}^3} \frac{d^3k}{(2\pi)^3} \frac{1}{2}\epsilon^{ijl}\epsilon^{lmn} \operatorname{Tr} \underline{\mathcal{S}}\Omega_{k_mk_n}E_j, \tag{63}$$

corresponding to the previously encountered spinor-Hall (or spin-Hall, depending on the chosen degree of freedom) response [cf. Eq. (44)], that relates the application of an electric field to a perpendicular spinor current with proportionality constant the first spinor-Chern number in momentum space. At second order, the corrections are given by

$$\tfrac{1}{2}\epsilon^{ilm}(E_m\partial_{r_i}\theta + B_{lm}\dot{\theta}), \tag{64}$$

where

$$\theta = \int_{\mathbb{T}^3} \frac{d^3k}{(2\pi)^3} \frac{1}{2}\epsilon^{lmn} \operatorname{Tr} \underline{\mathcal{S}}\Omega_{k_lk_m}A_{k_n} \tag{65}$$

is dubbed the "spinor-axion index." Similar to the usual charge responses due to a nontrivial axion field [14], the simultaneous application of an external electric (magnetic) field and the spatial (temporal) modulations of the Hamiltonian induce a nontrivial spinor current that depends on the gradient (rate of change) of the spinor-axion field—a topological property of the combined momentum-position-time coordinates. Hereafter, we omit corrections induced by electromagnetic fields as their contribution to the spinor transport is simply given by Eqs. (63) and (64), averaged over the corresponding volume of phase space.

Integrating the spinor current in the ith direction over a full pump cycle we obtain the spinor transport

$$\Delta q^i_{\hat{\mathcal{S}}} = \int_{T,V} dtd^3r j^i_{\hat{\mathcal{S}}} = c^i_1 - c^i_2 + c^i_3, \tag{66}$$

where the integral runs over a period T and the volume of the unit cell V (both set to unity for simplicity). The first two contributions are already derived in the context of one- and two-dimensional systems [cf. Eqs. (29) and (45)] and in three dimensions are proportional to the first and second sub-spinor-Chern numbers, namely,

$$c^i_1 = \int_{T,V,\mathbb{T}^3} \frac{dtd^3rd^3k}{(2\pi)^3} \operatorname{Tr} \underline{\mathcal{S}}\Omega_{tk_i} \tag{67}$$

and

$$c^i_2 = \int_{T,V,\mathbb{T}^3} \frac{dtd^3rd^3k}{(2\pi)^3} \epsilon^{ijk}\epsilon^{klm} \operatorname{Tr} \underline{\mathcal{S}}\Omega_{tk_l}\Omega_{r_jk_m}. \tag{68}$$

In addition to these responses, at third order in perturbation theory we obtain a third spinor-Chern number response, defined as

$$c_3^i = \int_{T,V,\mathbb{T}^3} \frac{dtd^3rd^3k}{(2\pi)^3}\frac{1}{2}\epsilon^{ijk}\epsilon^{lmn}\,\mathrm{Tr}\,\underline{\mathcal{S}}\Omega_{tk_l}\Omega_{r_jk_m}\Omega_{r_kk_n}. \quad (69)$$

The above expression is indeed the third spinor-Chern number characterizing the $(\boldsymbol{r},\boldsymbol{k},t)$ phase space since contributions from electromagnetic fields are assumed to be vanishing.

Before specifying the Hamiltonian, the derived expression of spinor transport, Eq. (66), can be decomposed as the temporal gradient of the spinor-dipole moment density, the second derivative of the spinor-quadrupole moment, and the third derivative of the spinor-octupole moment:

$$j^i_{\hat{\mathcal{S}}} = \partial_t\mathcal{P}^{\hat{\mathcal{S}}}_i - \partial_t\partial_{r_j}\mathcal{Q}^{\hat{\mathcal{S}}}_{ij}(\mathbf{r}) + \tfrac{1}{2}\partial_t\partial_{r_j}\partial_{r_l}\mathcal{O}^{\hat{\mathcal{S}}}_{ijl}(\mathbf{r}), \quad (70)$$

where $\boldsymbol{\mathcal{P}}^{\hat{\mathcal{S}}}$, $\mathcal{Q}^{\hat{\mathcal{S}}}_{ij}$, and $\mathcal{O}^{\hat{\mathcal{S}}}_{ijl}$ are the spinor analogs of the electric dipole, quadrupole, and octupole moment densities (cf. Appendix B). This decomposition can be used as an alternative definition of the spinor-multipole moments,

$$c^i_1 - c^i_2 + c^i_3 \overset{!}{=} \int_{T,V} dtd^3r\left(\partial_t\mathcal{P}^{\hat{\mathcal{S}}}_i - \partial_t\partial_{r_j}\mathcal{Q}^{\hat{\mathcal{S}}}_{ij} + \frac{1}{2}\partial_t\partial_{r_j}\partial_{r_l}\mathcal{O}^{\hat{\mathcal{S}}}_{ijl}\right), \quad (71)$$

i.e., integrated differences of spinor-multipole moments are determined by the spinor topological properties of phase space.

Focusing on the particular three-dimensional model of Eq. (58), the topological aspects of phase space become nonvanishing when $\boldsymbol{\phi}$ is a function of both space and time. Specifically, we assume $\phi_x(t)$ is a function of only time and takes values in the interval $[0, 2\pi]$, while ϕ_y (ϕ_z) is a function of only x (y) and is smoothly varied between zero and 2π. In this case, the first and second sub-spinor-Chern numbers of the system vanish for both the charge and physical spin degree, i.e., for $\hat{\mathcal{S}} = \mathbb{1}\otimes\mathbb{1}\otimes\mathbb{1}\otimes\mathbb{1}$ or $\hat{\mathcal{S}} = \tau_z\otimes\mathbb{1}\otimes\mathbb{1}\otimes\mathbb{1}$, respectively, due to the anticommuting and traceless properties of the $\boldsymbol{\gamma}$ matrices. Equivalently, the third Chern number associated to the charge degree is also zero. The only nonvanishing contribution comes from the third spin-Chern number and is given by

$$\Delta q^i_{\hat{\mathcal{S}}} = \frac{15}{16\pi^3}\int_{\mathbb{T}^6} d^3kd^3\phi\,\delta_{iz} \times\hat{\mathbf{d}}\cdot(\partial_{k_x}\hat{\mathbf{d}}\wedge\partial_{k_y}\hat{\mathbf{d}}\wedge\partial_{k_z}\hat{\mathbf{d}}\wedge\partial_{\phi_x}\hat{\mathbf{d}}\wedge\partial_{\phi_y}\hat{\mathbf{d}}\wedge\partial_{\phi_z}\hat{\mathbf{d}}), \quad (72)$$

where $\hat{\boldsymbol{d}} = \boldsymbol{d}/|\boldsymbol{d}|$, the integration domain in the six-dimensional parameter space $(\boldsymbol{k},\boldsymbol{\phi})$ is given by the 6-torus $\mathbb{T}^6$, and δ_{ij} is the Dirac delta function; the last stems from the Jacobian $\dot{\phi}_i\partial_{r_x}\phi_j\partial_{r_y}\phi_k = (2\pi)^3\delta_{ix}\delta_{jy}\delta_{kz}$ of the transformation between the position-time manifold and the $\boldsymbol{\phi}$ parameter space. Note that the first nonzero contributions due to a spin-orbit interaction appear as second-order corrections (see Appendix D); hence, these are omitted from the calculation of the third spin-Chern flux. Equation (72) is an integer number determined by the winding of the mapping $\hat{\mathbf{d}}$ between the parameter space $\mathbb{T}^6$ and the 6-sphere. For our tight-binding model (58) and driving scheme considered in this section, the third spin-Chern number induces a quantized spin transport along the z direction that is equal to 4.

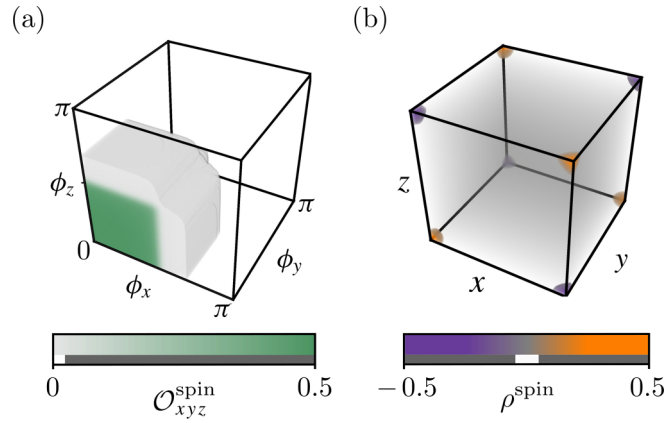

FIG. 8. Spin-octupole moment. (a) The spin-octupole moment (cf. Appendix B), as a function of the external parameters $\boldsymbol{\phi}$, takes values between zero (transparent) and 1/2 (green). The transition between the two values (gray region) is controlled by the chiral breaking mass h_0; i.e., the smaller it is, the sharper the transition. (b) The electronic ground state of the open boundary crystal at $\boldsymbol{\phi} = (0,0,0)$ exhibits spin localization at the corners, as expected from a nonvanishing spin-octupole moment. We note that the analogous expressions for the charge degree of freedom vanish independently of $\boldsymbol{\phi}$. For the simulations we have used $\Delta J^0_i/J_i = 0.1$, $h_0/J_i = 0.01$, and $\sum_i|\boldsymbol{\lambda}^i| = 0$.

The transport of physical spin due to the nontrivial winding number is reflected in the modulations of the spin-multipole moments, shown in Fig. 8(a). As a function of the external parameters, the spin-octupole moment takes continuous values and "winds" around singular points in the $\boldsymbol{\phi}$ parameter space. This leads to a nonzero third gradient and to a nontrivial contribution to spin current, as described by Eq. (70). We note that all other contributions from both electric and spin-multipole moments vanish, as expected from the trivial first and second spin-Chern numbers, as well as from the trivial Chern numbers [cf. Eq. (71)].

2. Accumulation

Here, we derive the spinor density using a semiclassical approach valid up to third order in perturbation theory. At first order, we find a set of first spinor-Chern fluxes in mixed momentum-position coordinates that are related to codimension-1 states, as already discussed in Sec. III A 2. In addition, we obtain the generalization of the Streda formula to three dimensions and the relation of spinor density to the first spinor-Chern number in momentum space. Second-order corrections are given by a set of second spinor-Chern fluxes in mixed momentum-position coordinates and give rise to codimension-2 states (cf. Sec. III B 2). Next are the spinor-axion field responses that depend on the applied electromagnetic fields, as well as on the deformation fields. Such corrections generalize the magnetoelectric effect [14] and relate spinor localization to the application of a parallel magnetic field. Finally, the third spinor-Chern flux appears as a unique third-order correction and is related to states with

codimensions 3. By extending the electric multipole description to spinor degrees of freedom and including effects up to the spinor-octupole moment, we establish a fundamental relation between boundary states, spinor-multipole moments, and the geometrical properties of phase space.

The spinor density of a generic 3D insulator under arbitrary perturbing fields is calculated using Eq. (5). As this expression contains numerous terms we first show the corrections that depend on the electromagnetic fields and then focus on pure deformation fields. Starting at first order, we obtain the 3D analog of the Streda formula, namely,

$$\int_{\mathbb{T}^3} \frac{d^3k}{(2\pi)^3} \frac{1}{2} \operatorname{Tr} \underline{\mathcal{S}} \Omega_{k_i k_j} B_{ij}, \tag{73}$$

that relates the spinor density to the applied magnetic field and to the first sub-spinor-Chern number in momentum space (cf. Sec. III B 2). Next, we derive the spinor-axion response

$$-\tfrac{1}{2}\epsilon^{ijk}\partial_{r_i}\theta B_{jk}, \tag{74}$$

that gives rise to a nonzero spinor density depending on the gradient of the spinor-axion field θ, defined in Eq. (65).

The remaining corrections due to deformation fields are given by

$$\rho_{\hat{\mathcal{S}}} = \int_{\mathbb{T}^3} \frac{d^3k}{(2\pi)^3} \operatorname{Tr} \underline{\mathcal{S}} \Bigg(-\sum_i \Omega_{r_i k_i} + \sum_i \frac{1}{6} \epsilon^{ikl} \epsilon^{imn} \times \Omega_{r_k k_m} \Omega_{r_l k_n} - \frac{1}{6} \epsilon^{ijk} \epsilon^{lmn} \Omega_{r_i k_l} \Omega_{r_j k_m} \Omega_{r_k k_n} \Bigg). \tag{75}$$

The first two terms have already been encountered in Secs. III A 2 and III B 2, albeit from a lower-dimensional perspective; in three dimensions, these terms can lead to helical surface and hinge states, respectively [57,63]. On the other hand, the last term in Eq. (75) is an intrinsically three-dimensional response as it depends on the full six-dimensional position-momentum manifold.

In the absence of electromagnetic fields, the accumulation of spinor charge in an arbitrary region $\mathcal{C}$ in position space is, hence, given by

$$q_{\hat{\mathcal{S}}} = \int_{\mathcal{C}} d^3 r \rho_{\hat{\mathcal{S}}} = -\sum_i \Phi_1^i + \sum_i \Phi_2^i - \Phi_3. \tag{76}$$

The first term defines a set of first spinor-Chern fluxes Φ_1^i in the (r_i, k_i) submanifold [cf. Eq. (13)],

$$\Phi_1^i = \int_{\mathcal{C},\mathbb{T}^3} \frac{d^3 r d^3 k}{(2\pi)^3} \operatorname{Tr} \underline{\mathcal{S}} \Omega_{r_i k_i}, \tag{77}$$

and induces a spinor accumulation with codimensions 1. Next is the second spinor-Chern flux Φ_2^i defined in a four-dimensional submanifold of phase space [cf. Eq. (14)],

$$\Phi_2^i = \int_{\mathcal{C},\mathbb{T}^3} \frac{d^3 r d^3 k}{(2\pi)^3} \frac{1}{6} \epsilon^{ikl} \epsilon^{imn} \operatorname{Tr} \underline{\mathcal{S}} \Omega_{r_k k_m} \Omega_{r_l k_n}. \tag{78}$$

Similar to the two-dimensional case [cf. Eq. (52)], the second spinor-Chern flux appears as a second-order correction and is related to states localized in two coordinates but extended in the remaining. Finally, at third order we obtain a unique three-dimensional response related to the third spinor-Chern flux,

$$\Phi_3 = \int_{\mathcal{C},\mathbb{T}^3} \frac{d^3 r d^3 k}{(2\pi)^3} \frac{1}{6} \epsilon^{ijk} \epsilon^{lmn} \operatorname{Tr} \underline{\mathcal{S}} \Omega_{r_i k_l} \Omega_{r_j k_m} \Omega_{r_k k_n}. \tag{79}$$

As the integration region $\mathcal{C}$ does not necessarily cover the entire parameter space, the corrections Φ_1, Φ_2, and Φ_3 are quantized only when additional symmetry constraints are imposed.

Focusing on our tight-binding model (58), the nontrivial geometrical properties of phase space manifest in the physical spin accumulation when the parameters $\boldsymbol{\phi}$ are properly modulated in space. Here, we assume that each ϕ_i is a function only of the associated position coordinate, i.e., $\partial_{r_i}\phi_j = 2\pi\delta_{ij}$, and takes values between zero and π within a finite region. Furthermore, we take $\mathcal{C}$ to be the support of the three-dimensional domain wall defined by the gradients of the external parameters $\boldsymbol{\phi}$. Calculating the corrections associated to the charge degree of freedom, i.e., taking $\hat{\mathcal{S}} = \mathbb{1}\otimes\mathbb{1}\otimes\mathbb{1}\otimes\mathbb{1}\otimes\mathbb{1}$, we find that all Chern fluxes vanish due to the anticommuting and traceless properties of $\boldsymbol{\gamma}$ matrices. Similarly, the first and second spin-Chern fluxes associated to physical spin, i.e., when $\hat{\mathcal{S}} = \tau_z \otimes \mathbb{1}\otimes\mathbb{1}\otimes\mathbb{1}\otimes\mathbb{1}$, evaluate to zero.

The only surviving term is the third spin-Chern flux, given by

$$\Phi_3 = \frac{15}{16\pi^3} \int_{\mathbb{T}^3\times[0,\pi]^3} d^3k d^3\phi \times \hat{\mathbf{d}} \cdot \left(\partial_{k_x}\hat{\mathbf{d}} \wedge \partial_{k_y}\hat{\mathbf{d}} \wedge \partial_{k_z}\hat{\mathbf{d}} \wedge \partial_{\phi_x}\hat{\mathbf{d}} \wedge \partial_{\phi_y}\hat{\mathbf{d}} \wedge \partial_{\phi_z}\hat{\mathbf{d}}\right), \tag{80}$$

where $\mathbb{T}^3 \times [0,\pi]^3$ is the integration domain in the six-dimensional parameter space $(\boldsymbol{k}, \boldsymbol{\phi})$, and we have used the Jacobian transformation $\partial_{r_x}\phi_i \partial_{r_y}\phi_j \partial_{r_z}\phi_k = (2\pi)^3 \delta_{ix}\delta_{jy}\delta_{kz}$ between position coordinates and the parameters $\boldsymbol{\phi}$. In our derivation, we have neglected the effects of a weak spin-orbit interaction $\boldsymbol{\lambda}^i$ since first-order corrections will vanish (see Appendix D). Equation (80) is determined by the covering of the map $\hat{\mathbf{d}}$ from the parameter space $(\boldsymbol{k}, \boldsymbol{\phi})$ to the 6-sphere and can be analytically calculated in the linearized regime around the points $(\boldsymbol{k}_0, \boldsymbol{\phi}_0) = (\pi, \pi, \pi, \pm\pi/2, \pm\pi/2, \pm\pi/2)$ as

$$\frac{60}{\pi^3} \int_0^\Lambda d^3\delta k d^3\delta\phi \frac{h_0}{\left(|\delta\boldsymbol{k}|^2 + |\delta\boldsymbol{\phi}|^2 + h_0^2\right)^{7/2}} \overset{\frac{h_0}{\Lambda}\to 0^+}{=} \frac{1}{2}, \tag{81}$$

where Λ is the cutoff energy and

$$\delta\boldsymbol{k} = (v_x k_x, v_y k_y, v_z k_z) \quad \text{and} \quad \delta\boldsymbol{\phi} = (u_x\phi_x, u_y\phi_y, u_z\phi_z)$$

are the linearized vectors with $v_i = J_i$ ($u_i = -2\Delta J_i^0$) the Fermi velocity along the k_i (ϕ_i) coordinate. When chiral symmetry is imposed to the tight-binding model, i.e., when $h_0/\Lambda \to 0$, the expression of the third spin-Chern flux becomes quantized and equal to $1/2$. As a result, the accumulation of spin at the 0D boundary defined by the domain wall becomes

$$|q_{\text{spin}}| = \tfrac{1}{2}. \tag{82}$$

Similar to Eq. (57) encountered in the 2D case, an alternative interpretation of the accumulated spin (and in general spinor degrees of freedom) is obtained by the classical theory

of multipole moments. Within this description, the spinor-Chern fluxes are related to the modulations of what we dub spinor-multipole moments:

$$-\sum_i \Phi_1^i + \sum_i \Phi_2^i - \Phi_3 \stackrel{!}{=} \int_V d^3r \left(-\partial_{r_i} \mathcal{P}_i^{\hat{s}} + \frac{1}{2}\partial_{r_i}\partial_{r_j}\mathcal{Q}_{ij}^{\hat{s}} - \frac{1}{6}\partial_{r_i}\partial_{r_j}\partial_{r_l}\mathcal{O}_{ijl}^{\hat{s}} \right). \quad (83)$$

Indeed, the bulk spin-octupole moment of the tight-binding model acquires nonzero values depending on the external parameters $\boldsymbol{\phi}$ (cf. Fig. 8). Around the high-symmetry points $\boldsymbol{\phi}_0 = (\pm\pi/2, \pm\pi/2, \pm\pi/2)$, the third gradient of the spin-octupole moment diverges depending on the value of the chiral breaking mass h_0; in the limit where $h_0/\Lambda \to 0$, its contribution to the spin density becomes quantized and equal to $1/2$, as predicted by Eq. (76) and the third spin-Chern flux given in Eq. (81). The remaining contributions from the spin-dipole and spin-quadrupole moments vanish, reflecting the trivial value of the first and second spin-Chern fluxes, respectively. Finally, we note that all contributions from the electric multipole moments are zero, as these are related to a trivial first, second, and third Chern flux.

IV. CONCLUSIONS

Designing realistic materials that can be easily controlled is of paramount importance when proposing experiments. Multiferroic materials provide a promising platform for controlling electronic properties with external electromagnetic and deformation fields [135]. In particular, ferromagnetic compounds with alternating crystal axes, such as Cu benzoate [117] and Yb_4As_3 [119], develop a staggered on-site potential when a perpendicular uniform magnetic field is applied and, as a consequence, the material becomes insulating. This is due to the competition between Dzyaloshinskii-Moriya interaction and a nonzero gyromagnetic tensor. The former can also give rise to an exchange interaction that depends on the applied electric field, as demonstrated in MnI_2 and oxides ABO_2 with $A =$ Cu, Ag, Li, or Na and $B =$ Cr or Fe [120–123]. More related to this paper, a highly efficient control of the antiferromagnetic order using a uniform magnetic field was demonstrated in two-dimensional latices of $SrIrO_3$ and $SrTiO_3$ [128].

Coupling electronic properties to strain offers an alternative route towards inducing controlled dynamics. Specifically, materials with piezoelectric, piezomagnetic, or flexoelectric properties develop nonzero electric and magnetic moments, such as polarization and magnetization, in response to strain [128,136–140]. Furthermore, symmetry analysis revealed an interesting class that combines electric and magnetic properties to give the "piezomagnetoelectric effect" [141,142]; i.e., the material develops a nonzero polarization due to a parallel magnetic field and strain. Enhanced piezomagnetoelectric properties were also observed in ceramics, rare-earth iron alloys, polymer composites [143,144], laminates [145–147], and epitaxial multilayers [148]. These materials have seen an enormous use in applications, both for their fundamental interest as well as their practicality.

Our semiclassical treatment of electrons in insulating crystals establishes a natural description of topological aspects, as it mostly arises from wave interference. As we have already shown, the nontrivial geometrical structure of phase space is fundamentally connected to macroscopic responses, namely, transport and accumulation. Such connection ultimately provides an alternative definition of the electric multipole moments in the form of integrated differences, thus eliminating any gauge ambiguity that can arise from the boundary conditions.

Introducing new internal quantum degrees of freedom augments the semiclassical description and leads to new topological constructs. This work provides an exhaustive delineation of such a generalized semiclassical theory, while deriving a set of multipoles with internal structure—the spinor-multipole moments. We believe that our work will inspire and guide novel solid-state studies both in real materials and quantum engineered systems. Of particular interest are the large-scale applications in quantum information technologies using qudits—a multilevel alternative to the conventional two-level qubit—that are expected to provide unprecedented storage capacity, processing power, and secure encryption, as well as reducing circuit complexity and increasing algorithm efficiency [149,150].

In this paper, we present a complete description of noninteracting electrons in weakly inhomogeneous, adiabatically driven insulators under external electromagnetic fields. We calculate the transport and accumulation of general spinor degrees of freedom using a semiclassical approach where we include corrections up to third order in perturbation theory. As such, we illustrate fundamental connections among geometry and physical observables that enable us to predict exotic states of matter. The derived effects are studied in concrete tight-binding models where the aforementioned relations are calculated both analytically and numerically. Remarkably, our approach puts topological spinor pumps, the spinor-Hall effect, spinor-higher-order TIs, spinor-multipole moments, and spinor-axion responses under the unifying umbrella of *phase-space topology*.

ACKNOWLEDGMENTS

We acknowledge useful discussions with Johannes Kellendonk. Work by I.P. is supported by the Early Postdoc mobility grant from the Swiss National Science Foundation (SNSF) under Project ID P2EZP2_199848. O.Z. is supported from the Deutsche Forschungsgemeinschaft (DFG), Project No. 449653034.

APPENDIX A: WAVE-PACKET CONSTRUCTION

We start by formally expanding the Hamiltonian in distances $\delta\hat{\boldsymbol{r}} = \hat{\boldsymbol{r}} - \boldsymbol{r}$ around the center-of-mass position $\boldsymbol{r}$ as

$$\hat{H} = \hat{H}_0 + \hat{H}', \quad (A1)$$

where $\hat{H}_0 = \hat{H}(\boldsymbol{r}, \boldsymbol{k}, t)$ is the local Hamiltonian evaluated at the center-of-mass coordinates, and $\hat{H}'$ are higher-order corrections. For example, at third order this is given by (hereafter,

we take $\hbar = e = 1$)

$$\hat{H}' = \frac{\partial \hat{H}_0}{\partial r_i}\delta\hat{\boldsymbol{r}}^i + \frac{1}{2}\frac{\partial \hat{H}_0}{\partial r_i}\frac{\partial \hat{H}_0}{\partial r_j}\{\delta\hat{\boldsymbol{r}}^i, \delta\hat{\boldsymbol{r}}^j\} + \frac{1}{4}\frac{\partial \hat{H}_0}{\partial r_i}\frac{\partial \hat{H}_0}{\partial r_j}\frac{\partial \hat{H}_0}{\partial r_k}\{\{\delta\hat{\boldsymbol{r}}^i, \delta\hat{\boldsymbol{r}}^j\}, \delta\hat{\boldsymbol{r}}^k\}. \tag{A2}$$

Regardless of their physical origins, the strength of these corrections eventually determines the choice of basis for the construction of the wave packet. Specifically, the size of the wave packet must be much smaller than the characteristic length scale defined by the $\hat{H}'$, both in position and momentum space (see Fig. 1). Constructing a wave packet that is several orders of magnitude larger than the lattice constant ensures a local basis of states with well-defined center-of-mass phase-space coordinates $(\boldsymbol{r}, \boldsymbol{k})$, and where intermediate length scales are encoded perturbatively up to a sufficiently large order. Any other strong corrections are included intrinsically in the local Hamiltonian $\hat{H}_0$ [70,74].

Concretely, the wave packet is built directly from the N eigenstates $\{|n(\boldsymbol{k}, \boldsymbol{r})\rangle\}$ of a set of isolated energy bands of $\hat{H}$ up to a particular order [50,68,73,91,92]; e.g., at second order in perturbation theory, the eigenstates are expanded as

$$|n\rangle \approx |n_0\rangle + |n'\rangle + |n''\rangle + \cdots, \tag{A3}$$

where $|n_0\rangle$ are the eigenstates of $\hat{H}_c$ and $|n'\rangle$ ($|n''\rangle$) are the first-order (second-order) corrections. Such terms modify significantly the structure of the wave packet and are, therefore, included in the derivation of the equations of motion. The wave packet is, thus, constructed as

$$|W_0\rangle := \int_{\mathbb{T}^d} d^d\mathrm{k} w(\boldsymbol{k}, t) \sum_n \eta_n e^{i\theta^{nm}(\boldsymbol{k},t)} |m(\boldsymbol{k}, \boldsymbol{r})\rangle, \tag{A4}$$

where $w(\boldsymbol{k}, t)$ is now the distribution function, $|\eta_n|^2 = 1$ is the probability of a particle being in the nth energy band, $\theta(\boldsymbol{k}, t) = \int_0^t \mathcal{E}^{nm}(\boldsymbol{k})dt' + \gamma^{nm}(t)$ is the sum of the dynamical phase given by the temporal integral over the perturbed energy dispersion $\mathcal{E}^{nm} = \langle n(\boldsymbol{k}, \boldsymbol{r})|\hat{H}_0 + \hat{H}'|m(\boldsymbol{k}, \boldsymbol{r})\rangle$, and the geometrical phase is $\gamma^{nm} = -i\int_0^t \mathcal{A}_t^{nm}dt'$ with $\mathcal{A}_t^{nm} := i\langle n(\boldsymbol{k})|\frac{d}{dt}|n(\boldsymbol{k})\rangle$. The center-of-mass position $\boldsymbol{r}$ and momentum $\boldsymbol{k}$ of this wave packet are defined as [69]

$$\boldsymbol{r} := \langle W_0|\hat{\boldsymbol{r}}|W_0\rangle \equiv \mathrm{Tr}\,\underline{\boldsymbol{r}} \quad \text{and} \quad \boldsymbol{k} := \langle W_0|\hat{\boldsymbol{k}}|W_0\rangle \equiv \mathrm{Tr}\,\underline{\boldsymbol{k}}, \tag{A5}$$

where $\underline{\boldsymbol{r}}$ and $\underline{\boldsymbol{k}}$ are the matrix representations of the position and momentum operator. In the case of a single occupied band, $\underline{\boldsymbol{r}}$ and $\underline{\boldsymbol{k}}$ become real numbers and the trace is omitted.

APPENDIX B: SPINOR-MULTIPOLE MOMENTS

In this section we review the definition of Wilson loops and nested Wilson loops, as well as defining their spinor analogs. These are ultimately related to the spinor-multipole moments, e.g., the spinor-dipole, spinor-quadrupole, and spinor-octupole moments. The notation used hereafter should be taken only with respect to this Appendix.

The Wilson loop, defined as

$$\mathcal{W}_\mu = e^{i\int \frac{d\boldsymbol{k}}{2\pi}\mathcal{A}_\mu}, \tag{B1}$$

is constructed by integrating the connection $\mathcal{A}_\mu^{nm} = \langle\psi^n(\boldsymbol{k})|i\partial_{k_\mu}|\psi^m(\boldsymbol{k})\rangle$ over the entire Brillouin zone. Its eigenvalues are related to the electronic positions relative to the positively charged atomic centers, also known as Wannier centers,

$$\mathcal{W}_\mu\big|w_\mu^n(\boldsymbol{k})\big\rangle = e^{i2\pi w_\mu^n}\big|w_\mu^n(\boldsymbol{k})\big\rangle, \tag{B2}$$

where $\{w_\mu^n\}$ is a set of Wannier centers in the μ direction with associated eigenvectors $|w_\mu^n(\boldsymbol{k})\rangle$. The electric dipole moment density is determined by the displacement of electrons from their atomic centers, i.e.,

$$\mathcal{P}_\mu = -\frac{i}{2\pi}\log\det\mathcal{W}_\mu. \tag{B3}$$

The nested Wilson loop is defined as

$$\mathcal{W}_{\mu\nu}^\pm = e^{i\int \frac{d\boldsymbol{k}}{2\pi}\mathcal{A}_{\mu\nu}^\pm}. \tag{B4}$$

The connection $[\mathcal{A}_{\mu\nu}^\pm]^{nm} = \langle u_\nu^n(\boldsymbol{k})|\partial_{k_\mu}|u_\nu^m(\boldsymbol{k})\rangle$ is defined over the so-called Wilson bands $|u_\mu^n(\boldsymbol{k})\rangle = \sum_i |w_\mu^n(\boldsymbol{k})\rangle^i|\psi^i(\boldsymbol{k})\rangle$, where $|w_\mu^n(\boldsymbol{k})\rangle^i$ is the ith component of the $\mathcal{W}_\mu$ Wilson loop eigenvector $|w_\mu^n(\boldsymbol{k})\rangle$. Here, the $\pm$ superscript denotes the Wannier sector that is comprised by either positive or negative eigenvalues. The electric quadrupole moment density is measured by the product of the averaged eigenvalues of nested Wilson loops, summed over the Wannier sectors:

$$\mathcal{Q}_{\mu\nu} = \frac{1}{(2\pi)^2}\sum_\sigma \log\det\mathcal{W}_{\mu\nu}^\sigma \log\det\mathcal{W}_{\nu\mu}^\sigma. \tag{B5}$$

The nested-nested Wilson loop is defined as

$$\mathcal{W}_{\mu\nu\rho}^\pm = e^{i\int \frac{d\boldsymbol{k}}{2\pi}\mathcal{A}_{\mu\nu\rho}^\pm}. \tag{B6}$$

The connection $[\mathcal{A}_{\mu\nu\rho}^\pm]^{nm} = \langle u_{\nu\rho}^n(\boldsymbol{k})|\partial_{k_\mu}|u_{\nu\rho}^m(\boldsymbol{k})\rangle$ is defined over the nested Wilson bands $|u_{\nu\rho}^n(\boldsymbol{k})\rangle = \sum_i |w_{\nu\rho}^n(\boldsymbol{k})\rangle^i|u_\rho^i(\boldsymbol{k})\rangle$, where $|w_{\nu\rho}^n(\boldsymbol{k})\rangle^i$ is the ith component of the $\mathcal{W}_{\nu\rho}$ nested-Wilson-loop eigenvector $|w_{\nu\rho}^n(\boldsymbol{k})\rangle$. The $\pm$ superscript denotes the nested Wannier sector that is comprised by either positive or negative eigenvalues of both Wilson and nested Wilson loops. The octupole moment is calculated by

$$\mathcal{O}_{\mu\nu\rho} = \frac{-i}{(2\pi)^3}\sum_\sigma \log\det\mathcal{W}_{\mu\nu\rho}^\sigma \log\det\mathcal{W}_{\rho\mu\nu}^\sigma \log\det\mathcal{W}_{\nu\rho\mu}^\sigma. \tag{B7}$$

We construct the spinor analog of the Wilson loop as

$$\mathcal{W}_\mu^{\hat{\mathcal{S}}} = e^{i\int \frac{d\boldsymbol{k}}{2\pi}S_\mu\mathcal{A}_\mu}, \tag{B8}$$

where $S_\mu^{nm} = \langle u_\mu^n(\boldsymbol{k})|\hat{\mathcal{S}}|u_\mu^m(\boldsymbol{k})\rangle$ are the components of the spinor operator $\hat{\mathcal{S}}$ in the basis of Wilson bands. The spinor-dipole moment is given by

$$\mathcal{P}_\mu^{\hat{\mathcal{S}}} = -\frac{i}{2\pi}\log\det\mathcal{W}_\mu^{\hat{\mathcal{S}}}. \tag{B9}$$

The spinor nested Wilson loop is defined as

$$\mathcal{W}_{\mu\nu}^{\pm,\hat{\mathcal{S}}} = e^{i\int \frac{d\boldsymbol{k}}{2\pi}S_{\mu\nu}\mathcal{A}_{\mu\nu}^\pm}, \tag{B10}$$

where $S_{\mu\nu}^{nm} = \langle u_{\mu\nu}^n(\boldsymbol{k})|\hat{\mathcal{S}}|u_{\mu\nu}^m(\boldsymbol{k})\rangle$ are the components of the spinor operator $\hat{\mathcal{S}}$ in the basis of nested Wilson bands $|u_{\mu\nu}^n(\boldsymbol{k})\rangle = \sum_i |w_{\mu\nu}^n(\boldsymbol{k})\rangle^i|u_\nu^i(\boldsymbol{k})\rangle$, where $|w_{\mu\nu}^n(\boldsymbol{k})\rangle^i$ is the ith

component of the $\mathcal{W}_{\mu\nu}$ nested-Wilson-loop eigenvector $|w^n_{\mu\nu}(\boldsymbol{k})\rangle$. The spinor-quadrupole moment is then given by

$$\mathcal{Q}^{\hat{\mathcal{S}}}_{\mu\nu} = \frac{1}{(2\pi)^2}\sum_{\sigma} \log\det \mathcal{W}^{\sigma,\hat{\mathcal{S}}}_{\mu\nu} \log\det \mathcal{W}^{\sigma,\hat{\mathcal{S}}}_{\nu\mu}. \quad \text{(B11)}$$

Finally, the spinor nested-nested Wilson loop is defined as

$$\mathcal{W}^{\pm,\hat{\mathcal{S}}}_{\mu\nu\rho} = e^{i\int \frac{dk}{2\pi} S_{\mu\nu\rho}\mathcal{A}^{\pm}_{\mu\nu\rho}}, \quad \text{(B12)}$$

where $S^{nm}_{\mu\nu\rho} = \langle u^n_{\mu\nu\rho}(\boldsymbol{k})|\hat{\mathcal{S}}|u^m_{\mu\nu\rho}(\boldsymbol{k})\rangle$ are the components of the spinor operator $\hat{\mathcal{S}}$ in the basis of nested-nested Wilson bands $|u^n_{\mu\nu\rho}(\boldsymbol{k})\rangle = \sum_i |w^n_{\mu\nu\rho}(\boldsymbol{k})\rangle^i |u^i_{\nu\rho}(\boldsymbol{k})\rangle$, where $|w^n_{\mu\nu\rho}(\boldsymbol{k})\rangle^i$ is the ith component of the $\mathcal{W}_{\mu\nu\rho}$ nested-nested Wilson loop eigenvector $|w^n_{\mu\nu\rho}(\boldsymbol{k})\rangle$. The spinor-octupole moment is calculated by

$$\mathcal{O}^{\hat{\mathcal{S}}}_{\mu\nu\rho} = \frac{-i}{(2\pi)^3}\sum_{\sigma} \log\det \mathcal{W}^{\sigma,\hat{\mathcal{S}}}_{\mu\nu\rho} \log\det \mathcal{W}^{\sigma,\hat{\mathcal{S}}}_{\rho\mu\nu} \log\det \mathcal{W}^{\sigma,\hat{\mathcal{S}}}_{\nu\rho\mu}. \quad \text{(B13)}$$

APPENDIX C: GENERALIZED EIGENVECTORS

Here, we derive the eigenvectors of general Hamiltonians that are given by the sum over anticommuting matrices. These are Hamiltonians of the form $\boldsymbol{d}\cdot\boldsymbol{\gamma} = \vec{d}\cdot\vec{\gamma} + m_0\gamma_0$, where $\{\gamma_\mu,\gamma_\nu\} = \delta_{\mu\nu}$ and γ_0 is the chiral matrix. Since the matrices can be brought into a block-diagonal form

$$H = \begin{pmatrix} H_+ & 0 \\ 0 & H_- \end{pmatrix}, \quad \text{(C1)}$$

where the spin operator is diagonal, we can analyze each subblock individually. Each subblock H_σ of spin $\sigma = \pm$ can be written as

$$H_\sigma = \begin{pmatrix} \sigma m_0 \mathbb{1} & \boldsymbol{q} \\ \boldsymbol{q}^\dagger & -\sigma m_0 \mathbb{1} \end{pmatrix}, \quad \text{(C2)}$$

where $\boldsymbol{q}$ is a hypercomplex number

$$\boldsymbol{q} = \vec{d}\cdot\hat{\vec{f}}, \quad \text{(C3)}$$

with $\hat{\vec{f}}$ its basis. In the 1D Hamiltonian of Eq. (22), this is simply the basis of complex numbers, i.e., $\hat{\vec{f}} = \{1, i\}$. In the 2D Hamiltonian of Eq. (42), it is given by quaternions, i.e., $\hat{\vec{f}} = \{\mathbb{1}, i\vec{\sigma}\}$, where $\vec{\sigma} = \{\sigma_x,\sigma_y,\sigma_z\}$ are the Pauli matrices. In the 3D Hamiltonian (58), the correct basis is $\hat{\vec{f}} = \{\vec{\sigma}\otimes\mathbb{1}, i\mathbb{1}\otimes\vec{\sigma}\}$.

The eigenvalues of H_σ can be found by taking the square root of the eigenvalues of its square

$$H^2_\sigma = \begin{pmatrix} m_0^2\mathbb{1} + \boldsymbol{q}\boldsymbol{q}^\dagger & 0 \\ 0 & m_0^2\mathbb{1} + \boldsymbol{q}^\dagger\boldsymbol{q} \end{pmatrix}, \quad \text{(C4)}$$

where $\boldsymbol{q}\boldsymbol{q}^\dagger = \boldsymbol{q}^\dagger\boldsymbol{q} = |\vec{d}|^2$ is given by the properties of the hypercomplex basis $\hat{\vec{f}}$. The eigenvalues are, hence,

$$\mathcal{E}^\pm = \pm\sqrt{m_0^2 + |\vec{d}|^2}, \quad \text{(C5)}$$

where each eigenvalue is $\frac{N}{2}$-fold-degenerate, with N the dimensions of the matrix H_σ. The corresponding eigenvectors are given by

$$\psi^\pm_\sigma = \mathcal{N}\begin{pmatrix} \frac{\boldsymbol{q}}{\mathcal{E}^\pm - \sigma m_0} v \\ v \end{pmatrix}, \quad \text{(C6)}$$

where $\mathcal{N} = \sqrt{\frac{\mathcal{E}^\pm - \sigma m_0}{2\mathcal{E}^\pm}}$ is a normalization factor, and v are the $\frac{N}{2}$ eigenvectors of $\boldsymbol{q}^\dagger\boldsymbol{q}$.

APPENDIX D: CORRECTIONS DUE TO SPIN-ORBIT INTERACTION

Here, we derive the first-order corrections due to a nonzero spin-orbit interaction and show that these vanish when the spinor operator $\hat{\mathcal{S}}$ commutes with the unperturbed Hamiltonian. The notation used hereafter should be taken only with respect to this Appendix. We use standard degenerate perturbation theory and assume that the general Hamiltonian is given up to first order,

$$H \approx H_0 + H', \quad \text{(D1)}$$

where $H' = \boldsymbol{D}\cdot\boldsymbol{\Gamma}$ is the Hamiltonian representing the spin-orbit interaction in arbitrary dimensions. We seek solutions of the form

$$|\tilde{n}^{(\alpha)}\rangle \approx |n^{(\alpha)}\rangle + |n'^{(\alpha)}\rangle, \quad \text{(D2)}$$

where $|n^{(\alpha)}\rangle$ is the nth set of g-fold-degenerate eigenstates of the unperturbed Hamiltonian, i.e., $H_0|n^{(\alpha)}\rangle = \mathcal{E}_n|n^{(\alpha)}\rangle$, with $\alpha \in \{1,2,\ldots,g\}$.

We rewrite the first-order corrections to the eigenstates as a sum of all unperturbed states,

$$|n'^{(\alpha)}\rangle = \sum_m c^{\alpha\beta}_{mn}|m^{(\beta)}\rangle, \quad \text{(D3)}$$

with weights $c^{\alpha\beta}_{mn}$. Substituting this in the eigenvalue equation, we obtain

$$\begin{aligned} &H'|n^{(\alpha)}\rangle + \textstyle\sum_m H_0 c^{\alpha\beta}_{mn}|m^{(\beta)}\rangle \\ &= \textstyle\sum_m c^{\alpha\beta}_{mn}\mathcal{E}_n|m^{(\beta)}\rangle + \mathcal{E}'_n|n^{(\alpha)}\rangle. \end{aligned} \quad \text{(D4)}$$

We multiply from the left with an arbitrary state $\langle m^{(\alpha)}|$ (which is not from the degenerate subspace $\langle n^{(\alpha)}|$) and solve for $c^{\alpha\beta}_{nm}$:

$$c^{\beta\alpha}_{mn} = \frac{\langle m^{(\beta)}|H'|n^{(\alpha)}\rangle}{\mathcal{E}_n - \mathcal{E}_m} \equiv \frac{H'^{\beta\alpha}_{mn}}{\mathcal{E}_n - \mathcal{E}_m} \quad \text{for } m \neq n. \quad \text{(D5)}$$

The remaining coefficients can be readily derived from the normalization condition using the appropriate basis as $c^{\alpha\beta}_{nn} = 0$.

We now calculate the first-order corrections to the first spinor-Chern curvature (other geometrical quantities follow a similar procedure),

$$\tilde{\underline{\mathcal{S}}}\tilde{\Omega}_{\mu\nu} = \underline{\mathcal{S}}\Omega_{\mu\nu} + \delta\underline{\mathcal{S}}\Omega_{\mu\nu} + \underline{\mathcal{S}}\delta\Omega_{\mu\nu} + \cdots, \quad \text{(D6)}$$

where $\underline{\mathcal{S}}^{\alpha\beta}_{nm} = \langle n^{(\alpha)}|\hat{\mathcal{S}}|m^{(\beta)}\rangle$, and $\Omega_{\mu\nu}$ are the spinor charge and curvature evaluated using the unperturbed states. The first-order corrections $\delta\underline{\mathcal{S}}^{\alpha\beta}_{nm} = \langle n^{(\alpha)}|\hat{\mathcal{S}}|m'^{(\beta)}\rangle + \langle n'^{(\alpha)}|\hat{\mathcal{S}}|m^{(\beta)}\rangle$ and $\delta\Omega_{\mu\nu}$ are evaluated using the perturbed eigenstates. The

former can be generally written as

$$\delta\underline{\mathcal{S}}^{\beta\alpha}_{nm} = \sum_{l} c^{\beta\gamma}_{lm}\underline{\mathcal{S}}^{\alpha\gamma}_{nl} + \left(c^{\alpha\gamma}_{ln}\right)^{*}\underline{\mathcal{S}}^{\gamma\beta}_{lm}. \tag{D7}$$

Assuming that $\hat{\mathcal{S}}$ is a good quantum number, i.e., it commutes with the unperturbed Hamiltonian H_0, then $\underline{\mathcal{S}}^{\alpha\beta}_{nm} = s^{\alpha}_{n}\delta^{\alpha\beta}_{nm}$ is a diagonal matrix with eigenvalues s^{α}_{n}. As a consequence, the first-order corrections to the spinor charge of the occupied subspace vanish,

$$\delta\underline{\mathcal{S}}^{\alpha\beta}_{nn} = \left(s^{\alpha}_{n} - s^{\beta}_{n}\right)c^{\beta\alpha}_{nn} = 0, \tag{D8}$$

due to $c^{\alpha\beta}_{nn} = 0$. Similar arguments hold for $\delta\Omega_{\mu\nu}$, where first-order corrections to the connection $\mathcal{A}_{\xi_\mu}$ defined by the ground state vanish. Going to higher orders in the perturbation series, the first nonzero contributions appear at order $\sim(\frac{\lambda}{\Delta\mathcal{E}})^2$, where λ is the strength of the spin-orbit interaction and $\Delta\mathcal{E}$ is the band gap.

[1] M. Z. Hasan and C. L. Kane, *Colloquium:* Topological insulators, Rev. Mod. Phys. **82**, 3045 (2010).

[2] X.-L. Qi and S.-C. Zhang, Topological insulators and superconductors, Rev. Mod. Phys. **83**, 1057 (2011).

[3] T. Ozawa, H. M. Price, A. Amo, N. Goldman, M. Hafezi, L. Lu, M. C. Rechtsman, D. Schuster, J. Simon, O. Zilberberg, and I. Carusotto, Topological photonics, Rev. Mod. Phys. **91**, 015006 (2019).

[4] K. v. Klitzing, G. Dorda, and M. Pepper, New Method for High-Accuracy Determination of the Fine-Structure Constant Based on Quantized Hall Resistance, Phys. Rev. Lett. **45**, 494 (1980).

[5] D. J. Thouless, M. Kohmoto, M. P. Nightingale, and M. den Nijs, Quantized Hall Conductance in a Two-Dimensional Periodic Potential, Phys. Rev. Lett. **49**, 405 (1982).

[6] P. Streda, Theory of quantised Hall conductivity in two dimensions, J. Phys. C **15**, L717 (1982).

[7] J. Bellissard, Gap labelling theorems for Schrödinger operators, *From Number Theory to Physics* (Springer, Berlin, 1992), pp. 538–630.

[8] J. Bellissard, J. Kellendonk, and A. Legrand, Gap-labelling for three-dimensional aperiodic solids, C. R. Acad. Sci. Ser. I Math. **332**, 521 (2001).

[9] K. Shiozaki, M. Sato, and K. Gomi, Topological crystalline materials: General formulation, module structure, and wallpaper groups, Phys. Rev. B **95**, 235425 (2017).

[10] A. Kitaev, Periodic table for topological insulators and superconductors, AIP Conf. Proc. **1134**, 22 (2009).

[11] C.-K. Chiu, J. C. Y. Teo, A. P. Schnyder, and S. Ryu, Classification of topological quantum matter with symmetries, Rev. Mod. Phys. **88**, 035005 (2016).

[12] S. Ryu, A. P. Schnyder, A. Furusaki, and A. W. W. Ludwig, Topological insulators and superconductors: Tenfold way and dimensional hierarchy, New J. Phys. **12**, 065010 (2010).

[13] A. Altland and M. R. Zirnbauer, Nonstandard symmetry classes in mesoscopic normal-superconducting hybrid structures, Phys. Rev. B **55**, 1142 (1997).

[14] X.-L. Qi, T. L. Hughes, and S.-C. Zhang, Topological field theory of time-reversal invariant insulators, Phys. Rev. B **78**, 195424 (2008).

[15] J. C. Y. Teo and C. L. Kane, Topological defects and gapless modes in insulators and superconductors, Phys. Rev. B **82**, 115120 (2010).

[16] J. Kruthoff, J. de Boer, J. van Wezel, C. L. Kane, and R. J. Slager, Topological Classification of Crystalline Insulators through Band Structure Combinatorics, Phys. Rev. X **7**, 041069 (2017).

[17] L. Fu, Topological Crystalline Insulators, Phys. Rev. Lett. **106**, 106802 (2011).

[18] A. Alexandradinata, Z. Wang, and B. A. Bernevig, Topological Insulators from Group Cohomology, Phys. Rev. X **6**, 021008 (2016).

[19] J. Bellissard, D. J. L. Herrmann, and M. Zarrouati, Hull of aperiodic solids and gap labelling theorems, Dir. Math. Quasicryst. **13**, 207 (2000).

[20] Y. E. Kraus and O. Zilberberg, Quasiperiodicity and topology transcend dimensions, Nat. Phys. **12**, 624 (2016).

[21] M. Lohse, C. Schweizer, H. M. Price, O. Zilberberg, and I. Bloch, Exploring 4D quantum Hall physics with a 2D topological charge pump, Nature (London) **553**, 55 (2018).

[22] M. Lohse, C. Schweizer, O. Zilberberg, M. Aidelsburger, and I. Bloch, A Thouless quantum pump with ultracold bosonic atoms in an optical superlattice, Nat. Phys. **12**, 350 (2016).

[23] S. Nakajima, T. Tomita, S. Taie, T. Ichinose, H. Ozawa, L. Wang, M. Troyer, and Y. Takahashi, Topological Thouless pumping of ultracold fermions, Nat. Phys. **12**, 296 (2016).

[24] N. Goldman, J. C. Budich, and P. Zoller, Topological quantum matter with ultracold gases in optical lattices, Nat. Phys. **12**, 639 (2016).

[25] N. Cooper, J. Dalibard, and I. Spielman, Topological bands for ultracold atoms, Rev. Mod. Phys. **91**, 015005 (2019).

[26] F. Mei, G. Chen, N. Goldman, L. Xiao, and S. Jia, Topological magnon insulator and quantized pumps from strongly-interacting bosons in optical superlattices, New J. Phys. **21**, 095002 (2019).

[27] Y. E. Kraus, Y. Lahini, Z. Ringel, M. Verbin, and O. Zilberberg, Topological States and Adiabatic Pumping in Quasicrystals, Phys. Rev. Lett. **109**, 106402 (2012).

[28] M. Verbin, O. Zilberberg, Y. Lahini, Y. E. Kraus, and Y. Silberberg, Topological pumping over a photonic Fibonacci quasicrystal, Phys. Rev. B **91**, 064201 (2015).

[29] L. Lu, J. D. Joannopoulos, and M. Soljačić, Topological states in photonic systems, Nat. Phys. **12**, 626 (2016).

[30] A. B. Khanikaev and G. Shvets, Two-dimensional topological photonics, Nat. Photonics **11**, 763 (2017).

[31] W. A. Benalcazar, J. Noh, M. Wang, S. Huang, K. P. Chen, and M. C. Rechtsman, Higher-order topological pumping, Phys. Rev. B **105**, 195129 (2022).

[32] O. Zilberberg, S. Huang, J. Guglielmon, M. Wang, K. P. Chen, Y. E. Kraus, and M. C. Rechtsman, Photonic topological boundary pumping as a probe of 4D quantum Hall physics, Nature (London) **553**, 59 (2018).

[33] M. Serra-Garcia, V. Peri, R. Süsstrunk, O. R. Bilal, T. Larsen, L. G. Villanueva, and S. D. Huber, Observation of a phononic quadrupole topological insulator, Nature (London) **555**, 342 (2018).

[34] D. J. Apigo, K. Qian, C. Prodan, and E. Prodan, Topological edge modes by smart patterning, Phys. Rev. Mater. **2**, 124203 (2018).

[35] W. Cheng, E. Prodan, and C. Prodan, Demonstration of Dynamic Topological Pumping Across Incommensurate Acoustic Meta-Crystals, Phys. Rev. Lett. **125**, 224301 (2020).

[36] Y. Long and J. Ren, Floquet topological acoustic resonators and acoustic Thouless pumping, J. Acoust. Soc. Am. **146**, 742 (2019).

[37] Y. Xia, E. Riva, M. I. N. Rosa, G. Cazzulani, A. Erturl, F. Braghin, and M. Ruzzene, Experimental Observation of Temporal Pumping in Electro-mechanical Waveguides, Phys. Rev. Lett. **126**, 095501 (2021).

[38] I. H. Grinberg, M. Lin, C. Harris, W. A. Benalcazar, C. W. Peterson, T. L. Hughes, and G. Bahl, Robust temporal pumping in a magneto-mechanical topological insulator, Nat. Commun. **11**, 974 (2020).

[39] M. I. N. Rosa, R. K. Pal, J. R. F. Arruda, and M. Ruzzene, Edge States and Topological Pumping in Spatially Modulated Elastic Lattices, Phys. Rev. Lett. **123**, 034301 (2019).

[40] Y.-W. Tsai, Y.-T. Wang, P.-G. Luan, and T.-J. Yen, Topological phase transition in a one-dimensional elastic string system, Crystals **9**, 313 (2019).

[41] S. Liu, W. Gao, Q. Zhang, S. Ma, L. Zhang, C. Liu, Y. J. Xiang, T. J. Cui, and S. Zhang, Topologically protected edge state in two-dimensional Su-Schrieffer-Heeger circuit, Research **2019**, 8609875 (2019).

[42] C. W. Peterson, W. A. Benalcazar, T. L. Hughes, and G. Bahl, A quantized microwave quadrupole insulator with topologically protected corner states, Nature (London) **555**, 346 (2018).

[43] S. Imhof, C. Berger, F. Bayer, J. Brehm, L. W. Molenkamp, T. Kiessling, F. Schindler, C. H. Lee, M. Greiter, T. Neupert *et al.*, Topolectrical-circuit realization of topological corner modes, Nat. Phys. **14**, 925 (2018).

[44] M. Serra-Garcia, R. Süsstrunk, and S. D. Huber, Observation of quadrupole transitions and edge mode topology in an LC circuit network, Phys. Rev. B **99**, 020304(R) (2019).

[45] M. Ezawa, Electric circuit simulations of nth-Chern-number insulators in $2n$-dimensional space and their non-Hermitian generalizations for arbitrary n, Phys. Rev. B **100**, 075423 (2019).

[46] R. Yu, Y. X. Zhao, and A. P. Schnyder, 4D spinless topological insulator in a periodic electric circuit, Natl. Sci. Rev. **7**, 1288 (2020).

[47] Y. Su and S.-Z. Lin, Topological sliding moiré heterostructure, Phys. Rev. B **101**, 041113(R) (2020).

[48] D. J. Thouless, Quantization of particle transport, Phys. Rev. B **27**, 6083 (1983).

[49] Y. E. Kraus, Z. Ringel, and O. Zilberberg, Four-Dimensional Quantum Hall Effect in a Two-Dimensional Quasicrystal, Phys. Rev. Lett. **111**, 226401 (2013).

[50] I. Petrides, H. M. Price, and O. Zilberberg, Six-dimensional quantum Hall effect and three-dimensional topological pumps, Phys. Rev. B **98**, 125431 (2018).

[51] S. Ryu, C. Mudry, C.-Y. Hou, and C. Chamon, Masses in graphenelike two-dimensional electronic systems: Topological defects in order parameters and their fractional exchange statistics, Phys. Rev. B **80**, 205319 (2009).

[52] M. Lin and T. L. Hughes, Topological quadrupolar semimetals, Phys. Rev. B **98**, 241103 (2018).

[53] K. Hashimoto, X. Wu, and T. Kimura, Edge states at an intersection of edges of a topological material, Phys. Rev. B **95**, 165443 (2017).

[54] J. Langbehn, Y. Peng, L. Trifunovic, F. von Oppen, and P. W. Brouwer, Reflection-Symmetric Second-Order Topological Insulators and Superconductors, Phys. Rev. Lett. **119**, 246401 (2017).

[55] W. A. Benalcazar, B. A. Bernevig, and T. L. Hughes, Quantized electric multipole insulators, Science **357**, 61 (2017).

[56] L. Trifunovic and P. Brouwer, Higher-Order Bulk-Boundary Correspondence for Topological Crystalline Phases, Phys. Rev. X **9**, 011012 (2019).

[57] M. Geier, L. Trifunovic, M. Hoskam, and P. W. Brouwer, Second-order topological insulators and superconductors with an order-two crystalline symmetry, Phys. Rev. B **97**, 205135 (2018).

[58] D. Călugăru, V. Juričić, and B. Roy, Higher-order topological phases: A general principle of construction, Phys. Rev. B **99**, 041301(R) (2019).

[59] Y. Zhao, Y. Gao, and D. Xiao, Electric polarization in inhomogeneous crystals, Phys. Rev. B **104**, 144203 (2021).

[60] F. Schindler, A. M. Cook, M. G. Vergniory, Z. Wang, S. S. Parkin, B. A. Bernevig, and T. Neupert, Higher-order topological insulators, Sci. Adv. **4**, eaat0346 (2018).

[61] Z. Wang, B. J. Wieder, J. Li, B. Yan, and B. A. Bernevig, Higher-Order Topology, Monopole Nodal Lines, and the Origin of Large Fermi Arcs in Transition Metal Dichalcogenides $X\mathrm{Te}_2$ (X = Mo, W), Phys. Rev. Lett. **123**, 186401 (2019).

[62] M. Ezawa, Minimal model for higher-order topological insulators and phosphorene, Phys. Rev. B **98**, 045125 (2018).

[63] Z. Song, Z. Fang, and C. Fang, $(d-2)$-Dimensional Edge States of Rotation Symmetry Protected Topological States, Phys. Rev. Lett. **119**, 246402 (2017).

[64] J. May-Mann and T. L. Hughes, Topological dipole conserving insulators and multipolar responses, Phys. Rev. B **104**, 085136 (2021).

[65] A. Cerjan, M. Jürgensen, W. A. Benalcazar, S. Mukherjee, and M. C. Rechtsman, Observation of a Higher-Order Topological Bound State in the Continuum, Phys. Rev. Lett. **125**, 213901 (2020).

[66] J. Košata and O. Zilberberg, Second-order topological modes in two-dimensional continuous media, Phys. Rev. Res. **3**, L032029 (2021).

[67] S. A. A. Ghorashi, X. Hu, T. L. Hughes, and E. Rossi, Second-order Dirac superconductors and magnetic field induced Majorana hinge modes, Phys. Rev. B **100**, 020509 (2019).

[68] M.C. Chang and Qian Niu, Berry Phase, Hyperorbits, and the Hofstadter Spectrum, Phys. Rev. Lett. **75**, 1348 (1995).

[69] G. Sundaram and Q. Niu, Wave-packet dynamics in slowly perturbed crystals: Gradient corrections and Berry-phase effects, Phys. Rev. B **59**, 14915 (1999).

[70] D. Xiao, M. C. Chang, and Q. Niu, Berry phase effects on electronic properties, Rev. Mod. Phys. **82**, 1959 (2010).

[71] D. Xiao, J. Shi, D. P. Clougherty, and Q. Niu, Polarization and Adiabatic Pumping in Inhomogeneous Crystals, Phys. Rev. Lett. **102**, 087602 (2009).

[72] Y. Gao, S. A. Yang, and Q. Niu, Field Induced Positional Shift of Bloch Electrons and Its Dynamical Implications, Phys. Rev. Lett. **112**, 166601 (2014).

[73] H. M. Price, O. Zilberberg, T. Ozawa, I. Carusotto, and N. Goldman, Four-Dimensional Quantum Hall Effect with Ultracold Atoms, Phys. Rev. Lett. **115**, 195303 (2015).

[74] H. M. Price, O. Zilberberg, T. Ozawa, I. Carusotto, and N. Goldman, Measurement of Chern numbers through center-of-mass responses, Phys. Rev. B **93**, 245113 (2016).

[75] C. H. Lee, Y. Wang, Y. Chen, and X. Zhang, Electromagnetic response of quantum Hall systems in dimensions five and six and beyond, Phys. Rev. B **98**, 094434 (2018).

[76] M. Di Liberto, N. Goldman, and G. Palumbo, Non-Abelian Bloch oscillations in higher-order topological insulators, Nat. Commun. **11**, 5942 (2020).

[77] I. Petrides and O. Zilberberg, Higher-order topological insulators, topological pumps and the quantum Hall effect in high dimensions, Phys. Rev. Res. **2**, 022049(R) (2020).

[78] S. K. Watson, R. M. Potok, C. M. Marcus, and V. Umansky, Experimental Realization of a Quantum Spin Pump, Phys. Rev. Lett. **91**, 258301 (2003).

[79] S. Murakami, N. Nagaosa, and S.-C. Zhang, Dissipationless quantum spin current at room temperature, Science **301**, 1348 (2003).

[80] J. Sinova, D. Culcer, Q. Niu, N. A. Sinitsyn, T. Jungwirth, and A. H. MacDonald, Universal Intrinsic Spin Hall Effect, Phys. Rev. Lett. **92**, 126603 (2004).

[81] Y. K. Kato, R. C. Myers, A. C. Gossard, and D. D. Awschalom, Observation of the spin Hall effect in semiconductors, Science **306**, 1910 (2004).

[82] J. Wunderlich, B. Kaestner, J. Sinova, and T. Jungwirth, Experimental Observation of the Spin-Hall Effect in a Two-Dimensional Spin-Orbit Coupled Semiconductor System, Phys. Rev. Lett. **94**, 047204 (2005).

[83] O. Dubinkin and T. L. Hughes, Higher-order bosonic topological phases in spin models, Phys. Rev. B **99**, 235132 (2019).

[84] D. González-Cuadra, Higher-order topological quantum paramagnets, Phys. Rev. B **105**, L020403 (2022).

[85] P. Sharma and C. Chamon, Quantum Pump for Spin and Charge Transport in a Luttinger Liquid, Phys. Rev. Lett. **87**, 096401 (2001).

[86] E. R. Mucciolo, C. Chamon, and C. M. Marcus, Adiabatic Quantum Pump of Spin-Polarized Current, Phys. Rev. Lett. **89**, 146802 (2002).

[87] F. Zhou, Topological spin pumps: The effect of spin rotation on quantum pumps, Phys. Rev. B **70**, 125321 (2004).

[88] R. Shindou, Quantum spin pump in $s = 1/2$ antiferromagnetic chains–holonomy of phase operators in sine-Gordon theory, J. Phys. Soc. Jpn. **74**, 1214 (2005).

[89] L. Fu and C. L. Kane, Time reversal polarization and a Z_2 adiabatic spin pump, Phys. Rev. B **74**, 195312 (2006).

[90] E. Prodan and H. Schulz-Baldes, *Bulk and Boundary Invariants for Complex Topological Insulators From K-Theory to Physics*, (Springer, 2016).

[91] M.-C. Chang and Q. Niu, Berry phase, hyperorbits, and the Hofstadter spectrum: Semiclassical dynamics in magnetic Bloch bands, Phys. Rev. B **53**, 7010 (1996).

[92] D. Culcer, Y. Yao, and Q. Niu, Coherent wave-packet evolution in coupled bands, Phys. Rev. B **72**, 085110 (2005).

[93] R. Karplus and J. M. Luttinger, Hall effect in ferromagnetics, Phys. Rev. **95**, 1154 (1954).

[94] H. M. Price and N. R. Cooper, Mapping the Berry curvature from semiclassical dynamics in optical lattices, Phys. Rev. A **85**, 033620 (2012).

[95] M. Cominotti and I. Carusotto, Berry curvature effects in the Bloch oscillations of a quantum particle under a strong (synthetic) magnetic field, Europhys. Lett. **103**, 10001 (2013).

[96] M. Wimmer, H. M. Price, I. Carusotto, and U. Peschel, Experimental measurement of the Berry curvature from anomalous transport, Nat. Phys. **13**, 545 (2017).

[97] D. Xiao, J. Shi, and Q. Niu, Berry Phase Correction to Electron Density of States in Solids, Phys. Rev. Lett. **95**, 137204 (2005).

[98] C. Duval, Z. Horváth, P. A. Horvathy, L. Martina, and P. Stichel, Berry phase correction to electron density in solids and "exotic" dynamics, Mod. Phys. Lett. B **20**, 373 (2006).

[99] K. Y. Bliokh, On the Hamiltonian nature of semiclassical equations of motion in the presence of an electromagnetic field and Berry curvature, Phys. Lett. A Gen. At. Solid State Phys. **351**, 123 (2006).

[100] P. Gosselin, F. Ménas, A. Bérard, and H. Mohrbach, Semiclassical dynamics of electrons in magnetic Bloch bands: A Hamiltonian approach, Europhys. Lett. **76**, 651 (2006).

[101] R. Jackiw and C. Rebbi, Solitons with fermion number 1/2, Phys. Rev. D **13**, 3398 (1976).

[102] C.-Y. Hou, C. Chamon, and C. Mudry, Electron Fractionalization in Two-Dimensional Graphenelike Structures, Phys. Rev. Lett. **98**, 186809 (2007).

[103] D. M. Nenno, C. A. Garcia, J. Gooth, C. Felser, and P. Narang, Axion physics in condensed-matter systems, Nat. Rev. Phys. **2**, 682 (2020).

[104] M. König, H. Buhmann, L. W. Molenkamp, T. Hughes, C.-X. Liu, X.-L. Qi, and S.-C. Zhang, The quantum spin Hall effect: Theory and experiment, J. Phys. Soc. Jpn. **77**, 031007 (2008).

[105] X.-L. Qi, Y.-S. Wu, and S.-C. Zhang, Topological quantization of the spin Hall effect in two-dimensional paramagnetic semiconductors, Phys. Rev. B **74**, 085308 (2006).

[106] C. Xiao and Q. Niu, Conserved current of nonconserved quantities, Phys. Rev. B **104**, L241411 (2021).

[107] M. Aidelsburger, M. Lohse, C. Schweizer, M. Atala, J. T. Barreiro, S. Nascimbene, N. R. Cooper, I. Bloch, and N. Goldman, Measuring the Chern number of Hofstadter bands with ultracold bosonic atoms, Nat. Phys. **11**, 162 (2015).

[108] M. Tarnowski, F. N. Ünal, N. Fläschner, B. S. Rem, A. Eckardt, K. Sengstock, and C. Weitenberg, Characterizing topology by dynamics: Chern number from linking number, Nat. Commun. **10**, 1728 (2019).

[109] D. Tran, A. Dauphin, A. Grushin, P. Zoller, and N. Goldman, Probing topology by "heating": Quantized circular dichroism in ultracold atoms, Sci. Adv. **3**, e1701207 (2017).

[110] D. T. Tran, N. R. Cooper, and N. Goldman, Quantized Rabi oscillations and circular dichroism in quantum Hall systems, Phys. Rev. A **97**, 061602 (2018).

[111] L. Asteria, D. T. Tran, T. Ozawa, M. Tarnowski, B. S. Rem, N. Fläschner, K. Sengstock, N. Goldman, and C. Weitenberg, Measuring quantized circular dichroism in ultracold topological matter, Nat. Phys. **15**, 449 (2019).

[112] S.-C. Zhang and J. Hu, A four-dimensional generalization of the quantum Hall effect, Science **294**, 823 (2001).

[113] J. Fröhlich and B. Perdini, New applications of the chiral anomaly, *Mathematical Physics* (Imperial College Press, London, 2000), pp. 9–47.

[114] S. Sugawa, F. Salces-Carcoba, A. R. Perry, Y. Yue, and I. B. Spielman, Observation of a non-Abelian Yang monopole: From new Chern numbers to a topological transition, Science **360**, 1429 (2018).

[115] C.-E. Bardyn, S. D. Huber, and O. Zilberberg, Measuring topological invariants in small photonic lattices, New J. Phys. **16**, 123013 (2014).

[116] M. Nakahara, *Geometry, Topology and Physics* (IOP Publishing, Bristol, UK, 2003).

[117] I. Affleck and M. Oshikawa, Field-induced gap in Cu benzoate and other $S = 1/2$ antiferromagnetic chains, Phys. Rev. B **60**, 1038 (1999).

[118] F. D. M. Haldane, Nonlinear Field Theory of Large-Spin Heisenberg Antiferromagnets: Semiclassically Quantized Solitons of the One-Dimensional Easy-Axis Néel State, Phys. Rev. Lett. **50**, 1153 (1983).

[119] M. Kohgi, K. Iwasa, J.-M. Mignot, B. Fåk, P. Gegenwart, M. Lang, A. Ochiai, H. Aoki, and T. Suzuki, Staggered Field Effect on the One-Dimensional $S = \frac{1}{2}$ Antiferromagnet Yb_4As_3, Phys. Rev. Lett. **86**, 2439 (2001).

[120] H. J. Xiang, E. J. Kan, Y. Zhang, M.-H. Whangbo, and X. G. Gong, General Theory for the Ferroelectric Polarization Induced by Spin-Spiral Order, Phys. Rev. Lett. **107**, 157202 (2011).

[121] T. Kimura, J. C. Lashley, and A. P. Ramirez, Inversion-symmetry breaking in the noncollinear magnetic phase of the triangular-lattice antiferromagnet $CuFeO_2$, Phys. Rev. B **73**, 220401(R) (2006).

[122] S. Seki, Y. Yamasaki, Y. Shiomi, S. Iguchi, Y. Onose, and Y. Tokura, Impurity-doping-induced ferroelectricity in the frustrated antiferromagnet $CuFeO_2$, Phys. Rev. B **75**, 100403(R) (2007).

[123] S. Seki, Y. Onose, and Y. Tokura, Spin-Driven Ferroelectricity in Triangular Lattice Antiferromagnets $ACrO_2$ ($A = $ Cu, Ag, Li, or Na), Phys. Rev. Lett. **101**, 067204 (2008).

[124] M. Mochol-Grzelak, A. Dauphin, A. Celi, and M. Lewenstein, Efficient algorithm to compute the second Chern number in four dimensional systems, Quantum Sci. Technol. **4**, 014009 (2019).

[125] T. Fukui, Y. Hatsugai, and H. Suzuki, Chern numbers in discretized Brillouin zone: Efficient method of computing (spin) Hall conductances, J. Phys. Soc. Jpn. **74**, 1674 (2005).

[126] R. D. King-Smith and D. Vanderbilt, Theory of polarization of crystalline solids, Phys. Rev. B **47**, 1651 (1993).

[127] W. A. Benalcazar, B. A. Bernevig, and T. L. Hughes, Electric multipole moments, topological multipole moment pumping, and chiral hinge states in crystalline insulators, Phys. Rev. B **96**, 245115 (2017).

[128] L. Hao, D. Meyers, H. Suwa, J. Yang, C. Frederick, T. R. Dasa, G. Fabbris, L. Horak, D. Kriegner, Y. Choi *et al.*, Giant magnetic response of a two-dimensional antiferromagnet, Nat. Phys. **14**, 806 (2018).

[129] Y. Gao, S. A. Yang, and Q. Niu, Geometrical effects in orbital magnetic susceptibility, Phys. Rev. B **91**, 214405 (2015).

[130] C. Xiao, Y. Ren, and B. Xiong, Adiabatically induced orbital magnetization, Phys. Rev. B **103**, 115432 (2021).

[131] C. Xiao, H. Liu, W. Wu, H. Wang, Q. Niu, and S. A. Yang, Intrinsic Nonlinear Electric Spin Generation in Centrosymmetric Magnets, Phys. Rev. Lett. **129**, 086602 (2022).

[132] C. Xiao and Q. Niu, Unified bulk semiclassical theory for intrinsic thermal transport and magnetization currents, Phys. Rev. B **101**, 235430 (2020).

[133] F. Liu, H.-Y. Deng, and K. Wakabayashi, Helical Topological Edge States in a Quadrupole Phase, Phys. Rev. Lett. **122**, 086804 (2019).

[134] C. Fang and L. Fu, New classes of topological crystalline insulators having surface rotation anomaly, Sci. Adv. **5**, eaat2374 (2019).

[135] W. Eerenstein, N. D. Mathur, and J. F. Scott, Multiferroic and magnetoelectric materials, Nature (London) **442**, 759 (2006).

[136] S. M. Kogan, Piezoelectric effect during inhomogeneous deformation and acoustic scattering of carriers in crystals, Sov. Phys. Solid State **5**, 2069 (1964).

[137] V. Gopalan, V. Dierolf, and D. A. Scrymgeour, Defect–domain wall interactions in trigonal ferroelectrics, Annu. Rev. Mater. Res. **37**, 449 (2007).

[138] P. Zubko, G. Catalan, and A. K. Tagantsev, Flexoelectric effect in solids, Annu. Rev. Mater. Res. **43**, 387 (2013).

[139] A. K. Tagantsev, Piezoelectricity and flexoelectricity in crystalline dielectrics, Phys. Rev. B **34**, 5883 (1986).

[140] P. V. Yudin and A. K. Tagantsev, Fundamentals of flexoelectricity in solids, Nanotechnology **24**, 432001 (2013).

[141] H. Grimmer, The piezomagnetoelectric effect, Acta Crystallogr., Sect. A: Found. Crystallogr. **48**, 266 (1992).

[142] Y. Benveniste, Magnetoelectric effect in fibrous composites with piezoelectric and piezomagnetic phases, Phys. Rev. B **51**, 16424 (1995).

[143] A. Van Run, D. R. Terrell, and J. H. Scholing, An in situ grown eutectic magnetoelectric composite material, J. Mater. Sci. **9**, 1710 (1974).

[144] C.-W. Nan, L. Liu, N. Cai, J. Zhai, Y. Ye, Y. H. Lin, L. J. Dong, and C. X. Xiong, A three-phase magnetoelectric composite of piezoelectric ceramics, rare-earth iron alloys, and polymer, Appl. Phys. Lett. **81**, 3831 (2002).

[145] J. Ryu, A. V. Carazo, K. Uchino, and H.-E. Kim, Magnetoelectric properties in piezoelectric and magnetostrictive laminate composites, Jpn. J. Appl. Phys. **40**, 4948 (2001).

[146] N. Cai, C.-W. Nan, J. Zhai, and Y. Lin, Large high-frequency magnetoelectric response in laminated composites of piezoelectric ceramics, rare-earth iron alloys and polymer, Appl. Phys. Lett. **84**, 3516 (2004).

[147] G. Srinivasan, E. T. Rasmussen, J. Gallegos, R. Srinivasan, Y. I. Bokhan, and V. M. Laletin, Magnetoelectric bilayer and multilayer structures of magnetostrictive and piezoelectric oxides, Phys. Rev. B **64**, 214408 (2001).

[148] M. K. Lee, T. K. Nath, C.-B. Eom, M. C. Smoak, and F. Tsui, Strain modification of epitaxial perovskite oxide thin films using structural transitions of ferroelectric $BaTiO_3$ substrate, Appl. Phys. Lett. **77**, 3547 (2000).

[149] E. Moreno-Pineda, C. Godfrin, F. Balestro, W. Wernsdorfer, and M. Ruben, Molecular spin qudits for quantum algorithms, Chem. Soc. Rev. **47**, 501 (2018).

[150] Y. Wang, Z. Hu, B. C. Sanders, and S. Kais, Qudits and high-dimensional quantum computing, Front. Phys. **8**, 479 (2020).